THESIS FOR THE DEGREE OF DOCTOR OF PHILOSOPHY

Microwave Detection for Large Vessel Occlusion

Seyed Moein Pishnamaz

CHALMERS
UNIVERSITY OF TECHNOLOGY

Department of Electrical Engineering
Chalmers University of Technology
Gothenburg, Sweden, 2025

Microwave Detection for Large Vessel Occlusion

Seyed Moein Pishnamaz
ISBN 978-91-8103-164-5

Acknowledgements, dedications, and similar personal statements in this thesis, reflect the author's own views.

Doktorsavhandlingar vid Chalmers tekniska högskola
Ny serie nr 5622
ISSN 0346-718X
Department of Electrical Engineering

Chalmers University of Technology
SE-412 96 Gothenburg, Sweden
Phone: +46 (0)31 772 1000
www.chalmers.se

Cover:
Front: Microwave antennas placed on a model of the head of a sheep that is undergoing a large vessel occlusion and a venous injection. The cerebral arterial occlusion and injection image were created using BioRender.com.
Back: Saving a brain from drowning with the help of microwaves. It was created using Dall-E.

Printed by Chalmers Reproservice
Gothenburg, Sweden, January 2025

To Shokoofeh

I'm not a mathematician, yet this resonates deeply with me:

.... the most rewarding part is the "Aha" moment, the excitement of discovery and enjoyment of understanding something new, the feeling of being on top of a hill, and having a clear view .... the beauty of mathematics only shows itself to more patient followers.

— Maryam Mirzakhani, 2008

Abstract

Stroke is the second leading cause of death worldwide, placing a substantial burden on patients and healthcare systems. Early treatment is crucial for patient outcomes, particularly in the case of large-vessel occlusions, where thrombectomy is indicated but only performed in a limited number of hospitals. Consequently, rapid and accurate prehospital detection is essential to expedite proper treatment.

This work proposes a microwave-based diagnostic approach enhanced by saline as a contrast enhancement agent to identify large-vessel occlusions. By exploiting the asymmetry in cerebral blood flow caused by partial or complete arterial blockage, the system detects conductivity variations via microwaves transmitted and received by antennas placed on the head. Three antennas are used, and a new dielectric rod antenna design is introduced to reduce multipath interference through surface waves. Compared to a self-grounded bow-tie antenna, the dielectric rod antenna decreases surface wave power by up to 10 dB and expands bandwidth by 72%.

An exploratory animal study was conducted to establish realistic measurement protocols for replicating large-vessel occlusions. Two signal processing algorithms were developed: one detects deviations based on signal power changes, and the other interprets these changes in the context of conductivity enhancement and pathophysiology. Data analysis demonstrated statistically significant changes in measured asymmetry due to saline injection, aligning with expected physiological responses.

These findings suggest that microwave-based prehospital detection of large vessel occlusions is feasible. The proposed method holds promise for improving stroke triage by enabling faster, more reliable identification of thrombectomy candidates, ultimately reducing treatment delays and improving patient outcomes.

Keywords: Stroke, Large Vessel Occlusion, Thrombectomy, Microwave, Antenna, Biomedical Signal Procsseing, Brain Edema.

List of Publications

This thesis is based on the following publications:

[A] **Seyed Moein Pishnamaz, Xuezhi Zeng, Hana Dobšíček Trefná, Mikael Persson, Andreas Fhager**, "Reducing Waves on the Body Surface in Near-Field Medical Diagnostics by a Dielectric Rod Antenna". IEEE Transactions on Antenna and Propagation.

[B] **Seyed Moein Pishanamz**, Andreas Fhager, Mikael Persson, "Analysis of the 2D Guided Mode Propagation in a 3D Dielectric Rod Antenna". EuCAP 2023.

[C] **Seyed Moein Pishnamaz, Xuezhi Zeng, Hana Dobšíček Trefná, Mikael Persson, Andreas Fhager**, "Asymmetry Detection in a Noisy Microwave-Based Biomedical Diagnosis". IMBioC 2024.

[D] **Seyed Moein Pishnamaz, Xuezhi Zeng, Hana Dobšíček Trefná, Mikael Persson, Andreas Fhager**, "Microwave-Based Detection of Large Vessel Occlusion Using Contrast Enhancement". To be Submitted to IEEE Transactions on Biomedical Engineering.

[E] **Seyed Moein Pishnamaz, Xuezhi Zeng, Hana Dobšíček Trefná, Mikael Persson, Andreas Fhager**, "Microwave-Based Detection of Large Vessel Occlusion Using Contrast Enhancement- A Frequency-Derivative Analysis". To be Submitted to IEEE Transactions on Biomedical Engineering.

[F] **Seyed Moein Pishnamaz, Xuezhi Zeng, Hana Dobšíček Trefná, Mikael Elam, Andreas Fhager, Mikael Persson**, "Investigating the Effects of Saline Injection as a Contrast Enhancement Agent in Microwave Diagnostics of Large Vessel Occlusion". To be Submitted to Stroke Translational Research.

Other publications by the author, not included in this thesis, are:

[G] **Seyed Moein Pishnamaz**, Mikael Persson, Andreas Fhager, "Determining the Electrical Conductivity of Blood as a Function of Salt Concentration

at 1 GHz". *BioEM2023*, THE 2ND ANNUAL CONFERENCE OF BioEM, 18–23 June 2023, Oxford, United Kingdom.

[H] **Seyed Moein Pishnamaz**, Xuezhi Zeng, Hana Dobsicek Trefna, Mikael Persson, Andreas Fhager, "A Dielectric Rod Antenna for Medical Diagnosis". *Swedish Microwave Days 2023*, 23–25 May 2023, Stockholm, Sweden.

[I] **Seyed Moein Pishnamaz**, Andreas Fhager, Mikael Persson, "Microwave Detection of The Shunt Malfunction in Hydrocephalus Children". *ESHO2022*, 34th Annual Meeting European Society for Hyperthermic Oncology, 14–17 September 2022, Gothenburg, Sweden.

[J] **Seyed Moein Pishnamaz**, Andreas Fhager, Mikael Persson, "Microwave Detection of The Shunt Malfunction in Hydrocephalus Children". *Medicinteknikdagarna* , 4-6 October 2022, Luleå, Sweden.

[K] **Seyed Moein Pishnamaz**, Elein Khaled, Miriam von Westphalen, Xuezhi Zeng, Mikael Persson, Andreas Fhager, "Microwave Diagnostics for Biomedical Applications". *Medicinteknikdagarna* , 8-10 October 2023, Stockholm, Sweden.

[L] **Seyed Moein Pishnamaz**, Xuezhi Zeng, Hana Dobsicek Trefna, Mikael Persson, Andreas Fhager, "Microwave Diagnostics for Neurological Disorders". *Medicinteknikdagarna* , 8-10 October 2024, Gothenburg, Sweden.

[M] **Seyed Moein Pishnamaz**, Mikael Persson, Andreas Fhager, "Microwave Detection of The Shunt Malfunction in Children with Brain Tumor and Hydrocephalus". *Journal Manuscript in Prepration.*

Acknowledgments

With this thesis, a significant chapter of my academic journey as a PhD student comes to an end—an achievement made possible only through the help and support of many people.

First and foremost, I would like to thank Mikael, my supervisor and examiner, for giving me the opportunity to be his PhD student. I am grateful for his unwavering support, his encouragement to learn and explore new topics, and his belief in me even when I doubted myself. I also owe much gratitude to Andreas, my supervisor for the past two years, for our many discussions, meticulous paper revisions, and excellent group management—thank you for always being there. A heartfelt thank-you goes out to Xuezhi, my co-supervisor, for assisting me with everything from hardware troubleshooting to delving deep into my mathematical formulations. I'm equally appreciative of Hana for her enthusiasm about our measurement campaigns and keen interest in medical topics, and of Mikael Elam for reviewing my medical manuscript and sharing his invaluable medical expertise. I also want to acknowledge our collaborators at the Norwegian University of Life Sciences—especially Marianne, Silje, Frode, and Snorre—for their cooperation and hospitality during our measurement campaigns.

I've been fortunate enough to turn colleagues into true friends. Thank you, Laura, Mattia, and Robin, for your unwavering assistance—be it in the lab, the office, or during afterworks. I'm also thankful for my friends in E2: Alejandra, Rita, Gabriel, Alvin, Rikard, Anna, Yara, Victor, André, Erik, and Kristian, who never failed to brighten my day. Special thanks go to Navid & Niloofar and Mohammad & Neda for the countless memorable moments we've shared. To my fellow Iranian friends—Javad, Mostafa, Zahra, Mehdi, Azam, Mohsen, Negar, Morteza, Narges, MohammadAli, Azadeh, Nima, Marziye, Fredows, Saeed, Reza, and Afsaneh—thank you for making this place feel like home. The list could go on, and I apologize to anyone I've inadvertently left out—you are equally cherished. Finally, I want to thank my family—Pedar, Maman, my brother Amin, and my parents-in-law—for their steadfast support throughout this journey. Last but certainly not least, to my best friend and the love of my life, Shokoofeh: words cannot express how much I cherish every moment with you. Thank you for everything.

Moein, January 2025, Gothenburg

Acronyms

LVO:	Large Vessel Occlusion
DRA:	Dielectric Rod Antenna
SGBTA:	Self-Grounded Bow-tie Antenna
CEA:	Contrast-Enhancing Agent
ISF:	Isotonic Filteration (Chapter 4)
AWW:	Accumulated Window Width
CSF:	Cerebospinal Fluid
ISF:	Interstitial Fluid (Chapter 5)
CCA:	Common Carotid Artery
VA:	Vertebral Artery
MAP:	Mean Arterial Pressure
CN:	Caudate Nucleus
CT:	Computed Tomography
HU:	Hounsfield Unit

Contents

Part I

Overview

CHAPTER 1

Introduction

Stroke is a leading global health concern, recognized as the second most common cause of death worldwide [1] and the third most significant contributor to disability-adjusted life years (DALYs) after ischaemic heart disease and lower respiratory infections [2]. A DALY quantifies the burden of disease by estimating the loss of time of full health. It is a common measure to quantify the impact of diseases, such as stroke [3]. These statistics underscore the substantial prevalence and debilitating consequences of stroke on individuals and societies.

In addition to its profound health implications, stroke imposes a significant economic burden. In Europe alone, the total cost associated with stroke was estimated at €64.1 billion in 2010 [4]. In the United States, the mean lifetime cost for an ischemic stroke patient is approximately $140,000 [5].

In summary, stroke is a significant contributor both to global mortality and disability, and it also imposes substantial economic and healthcare burdens. This underscores the critical need for effective prevention, early diagnosis, and appropriate treatment strategies. A deeper understanding of the pathophysiology and classification of stroke is fundamental to addressing these challenges.

Stroke is a condition characterized by insufficient blood flow to the brain

Figure 1.1: Schematic of different types of stroke. Left hemorrhagic and right ischemic. The red area on the left indicates a hemorrhagic (caused by bleeding) stroke, and the blue area on the right indicates an ischemic stroke (caused by a cloth) with deoxygenated brain tissue. Images are from [7].

and is broadly classified into two main types: ischemic and hemorrhagic. An ischemic stroke occurs when an occlusion blocks blood flow and constitutes the most common type, accounting for up to 85% of all stroke cases in Western countries such as Sweden [6]. The rest of the cases constitute hemorrhagic stroke, resulting from bleeding within the brain due to a ruptured vessel, as illustrated in Fig. 1.1.

The treatment options for ischemic and hemorrhagic strokes differ fundamentally. Thrombolysis, a life-saving intervention for ischemic stroke, dissolves the clot and restores blood flow. However, applying the same treatment to a patient with a hemorrhagic stroke can exacerbate bleeding, leading to serious and even fatal outcomes. Some ischemic strokes are caused by an occlusion in one of the larger arteries in the brain, denoted a large vessel occlusion (LVO). These patients could benefit from thrombectomy, a type of treatment where the clot is mechanically removed with the help of a catheter. Consequently, early and precise diagnosis of the stroke type is crucial for effective and safe management.

The importance of early and accurate stroke diagnosis cannot be overstated, as it is the foundation for timely and appropriate treatment. However, operational challenges, such as the lack of adequate prehospital triage systems,

further complicate the effective management of stroke patients. Without such systems, patients are often transported to the nearest hospital for initial assessment and diagnostics with imaging before any decisions are taken. Thrombectomy is not performed at smaller hospitals, and therefore patients with an LVO usually have to be transferred to thrombectomy-capable stroke centers—a process termed "drip and ship" [8]. Unfortunately, this approach can result in critical delays, jeopardizing patient outcomes.

These delays are particularly concerning for patients with LVO, a subtype of acute ischemic stroke that is associated with severe outcomes. LVO accounts for up to 30% of acute ischemic stroke cases but disproportionately contributes to over 90% of the acute ischemic stroke-related mortality [9]. The distribution of LVO and other ischemic stroke subtypes is depicted in Fig. 1.2. Lacunar stroke, a condition when a thrombosis blocks one of the small blood vessels deep in the brain, is the most common subtype with 37% of acute ischemic strokes. The LVO is the second most common type of ischemic stroke, accounting for 31%. Finally, cardiac embolis, which accounts for 22% of the ischemic strokes, is the condition where a blood clot is formed in the heart and travels through the bloodstream, causing an ischemic stroke. This, in fact, can also create LVO if the clot is large enough to block a large artery.

The critical role of timely intervention in ischemic stroke, particularly for patients with LVO, cannot be overstated. Thrombectomy offers significant benefits but is limited to specialized stroke centers [11]. Unfortunately, the current “drip and ship” approach often results in unnecessary delays, diminishing the chances of favorable outcomes. With every 10-minute reduction in treatment time translating to 39 additional days of disability-free life (Quality-adjusted life year, QALY, divided by 365) [12]. Improving prehospital triage to prioritize direct transport of LVO patients to advanced stroke centers is imperative.

To address these challenges, this thesis proposes a novel diagnostic method leveraging contrast enhancement agents and microwave detection. By introducing a saline-based contrast agent, the method artificially creates measurable differences in conductivity between the affected and unaffected regions of the brain. This innovative approach aims to simplify signal analysis and enhance diagnostic accuracy, enabling faster and more reliable differentiation of stroke types. Preliminary tests conducted on simulated data and animal

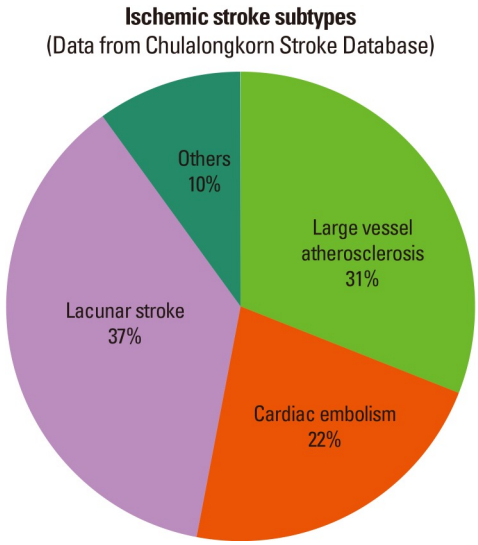

Figure 1.2: The distribution of the ischemic stroke subtypes [10].

models provide a foundation for further exploration, paving the way for future clinical applications.

1.1 Clinical Background

In this section, the medical diagnosis and treatment of stroke are discussed, with a focus on ischemic stroke, i.e. when a thrombosis (clot) obstructs an artery. Thrombolysis is a widely used treatment aimed at dissolving the clot [13]. For larger arterial blockages, thrombectomy is a highly effective interventional procedure [14] where a catheter is inserted into the cerebral arteries to mechanically remove the clot. In many parts of the world, thrombectomy can be performed up to 24 hours after stroke onset [15]. However, the procedure is more effective if administered at an early stage after onset.

However, access to thrombectomy is often limited to specialized hospitals. For instance, in the Region of Västra Götaland in Sweden, only Sahlgrenska University Hospital performs this procedure [16]. A recent study indicates that five times more patients could benefit from thrombectomy than are currently

treated [16], emphasizing the need for faster and more reliable prehospital diagnostics. Currently, the modified NIH stroke scale/score (mNIHSS) is a common tool used in ambulances to evaluate stroke severity based on clinical observations. However, the procedure relies on subjective assessments. This is a matter of debate if mNIHSS could be the sole basis for bypassing a primary stroke center to a comprehensive stroke center with endovascular capabilities [17]. It is therefore of interest to integrate subjective measures in order to improve patient triage. This would potentially decrease the time to appropriate treatment.

Microwave diagnostics has emerged as a valuable complement to existing diagnostic modalities [18]–[21]. Unlike ionizing X-rays used in computed tomography (CT), microwaves are non-ionizing, and the power level is as low as to allow for multiple measurements as well as monitoring. Advances in microwave technology, largely driven by developments in the telecommunications industry, have resulted in systems that are fast, compact, and cost-efficient [22]. Other prehospital diagnostic techniques, such as bioelectrical impedance [23] and near-infrared spectroscopy [24], also exist, but microwaves possess the unique advantage of detecting both superficial and deep targets [25]. A recent bibliometric analysis highlights microwave imaging as one of the top three modalities studied for prehospital stroke detection devices [26].

The following section discusses the principles of microwave diagnostics, illustrating its applications and methods. Subsequently, the two central terms of this thesis—"microwave" and "microwave diagnosis of stroke"—are clarified, establishing the connection between them and laying the foundation for the research presented.

1.2 Electromagnetic Waves

In this section, an introduction to electromagnetic (EM) waves is given. The propagation of EM waves is governed by well-known Maxwell's equations [27]. Maxwell's equation for the time-harmonic fields in the phasor notation is as

follows:

$$\nabla \cdot \bar{\mathbf{D}} = \rho \quad \text{Gauss's Law} \tag{1.1}$$
$$\nabla \cdot \bar{\mathbf{B}} = 0 \quad \text{Gauss's Law for Magnetism} \tag{1.2}$$
$$\nabla \times \bar{\mathbf{E}} = -j\omega\bar{\mathbf{B}} \quad \text{Faraday's Law of Induction} \tag{1.3}$$
$$\nabla \times \bar{\mathbf{H}} = j\omega\bar{\mathbf{D}} + \bar{\mathbf{J}} \quad \text{Ampere's Circuital Law} \tag{1.4}$$

where $\bar{\mathbf{D}}$ and $\bar{\mathbf{B}}$ are electric and magnetic flux density and $\bar{\mathbf{E}}$ and $\bar{\mathbf{H}}$ are the electric and magnetic field intensity respectively. Volume charge density is shown by ρ and surface current density $\bar{\mathbf{J}}$ is the sum of source currents $\bar{\mathbf{J}}_i$ and currents created because of the conduction in the material, $\bar{\mathbf{J}}_c$ which in the linear case is related to the electric field by the conductivity of the material σ, as is given in the equation below.

$$\bar{\mathbf{J}}_c = \sigma\bar{\mathbf{E}} \tag{1.5}$$

The relation between the flux density and the field intensity for a linear homogeneous isotropic material is as follows:

$$\bar{\mathbf{D}} = \epsilon_0\epsilon_r\bar{\mathbf{E}} \tag{1.6}$$
$$\bar{\mathbf{B}} = \mu_0\mu_r\bar{\mathbf{H}} \tag{1.7}$$

ϵ_0 and μ_0 are the permittivity and permeability of the vacuum respectively. ϵ_r and μ_r are the relative permittivity and relative permeability of the material where the EM wave is propagating. In a source-free, $\rho = 0$, $\bar{\mathbf{J}}_i = 0$, and nonmagnetic $\mu_r = 1$ medium Maxwell's equations reduce to:

$$\nabla \cdot \bar{\mathbf{E}} = 0 \tag{1.8}$$
$$\nabla \cdot \bar{\mathbf{H}} = 0 \tag{1.9}$$
$$\nabla \times \bar{\mathbf{E}} = -j\omega\mu_0\bar{\mathbf{H}} \tag{1.10}$$
$$\nabla \times \bar{\mathbf{H}} = j\omega\epsilon_0\epsilon_{rc}\bar{\mathbf{E}} \tag{1.11}$$

where ϵ_{rc} is the complex relative permittivity of the medium and is defined as:

$$\epsilon_{rc} = \epsilon_r + \frac{\sigma}{j\omega\epsilon_0}. \tag{1.12}$$

The wave equation can be derived from Maxwell's equations as:

$$\nabla^2\bar{\mathbf{E}} \quad + \quad \gamma^2\bar{\mathbf{E}} \quad = \quad 0 \tag{1.13}$$

The most simple solution to the wave equation is a 1-dimensional plane wave propagating in the z-direction.

$$\bar{\mathbf{E}} = (E_{x0}\hat{x} + E_{y0}\hat{y})e^{-j\gamma z} \tag{1.14}$$

γ can also be written as $\gamma = \beta - j\alpha$. In this case, β is the wave number and α is the attenuation constant in the lossy material.

When an EM wave propagates through a lossy medium, it inevitably loses power, which is absorbed and dissipated as heat. Additionally, significant interactions occur when the wave encounters a discontinuity—a boundary where the permittivity and conductivity of the medium change spatially. At such boundaries, two key phenomena, reflection and transmission, take place, as illustrated in Fig. 1.3. In a complex, multi-layered environment like the human body, the EM wave undergoes numerous reflections and transmissions, each altering its magnitude and phase.

These cumulative changes carry valuable information about the medium's properties and can be detected by a sensor, typically an antenna. The acquired signals are then processed using advanced signal processing algorithms to extract meaningful diagnostic insights. This principle forms the basis of all electromagnetic-based diagnostic methods, providing a robust foundation for exploring innovative approaches such as microwave-based diagnosis of stroke.

Microwaves, a subset of EM waves, span frequencies from 300 MHz to 300 GHz. Within this range, the lower-frequency band is particularly well-suited for biomedical applications. This is because waves in this lower band experience less attenuation when propagating through biological tissues, such as those in the human body, compared to higher-frequency microwaves [28]. This reduced attenuation enhances their ability to penetrate tissues and makes them more practical for diagnostic and therapeutic purposes in medical contexts.

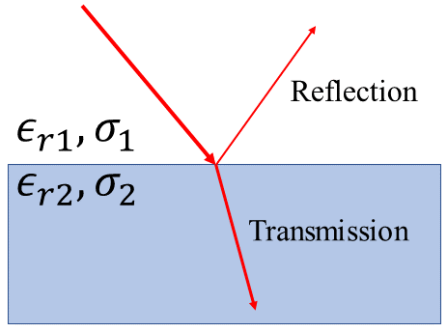

Figure 1.3: Interactions of the EM Waves with Materials

1.3 Microwave Diagnosis of Stroke

In a generic microwave diagnosis system, shown schematically in Fig. 1.4, multiple antennas (depicted as blue circles) operating at microwave frequencies surround the body (approximated here as a multi-layer ellipse). These antennas can be configured in various ways, such as mono-static, bi-static, or multi-static. In the multi-static scheme adopted in this work, one antenna transmits an EM wave while the other antennas receive; then, the transmitting antenna is switched until each antenna has transmitted once. The collected data take the form of scattering parameters [29], which capture how the medium alters the transmitted wave's magnitude and phase. Consequently, these parameters encode information about the dielectric properties of the tissues through which the wave has passed.

Physiological changes associated with certain diseases or traumas manifest as alterations in the electromagnetic characteristics of the affected tissue, and these changes can be detected by microwave-based methods. Several diagnostic applications leverage these dielectric contrasts, including microwave imaging of breast tumors [30]–[32], assessments of muscle quality [33], colonoscopy [34].

Another important diagnostic scenario for microwave-based methods is stroke detection, as depicted in Fig. 1.5. The image illustrates the wave propagation and reflection from a blood volume, originating from a hemorrhagic stroke. The permittivity of the blood pool differs from that of the surrounding brain tissue, the EM waves therefore reflect from the blood and thereby make it

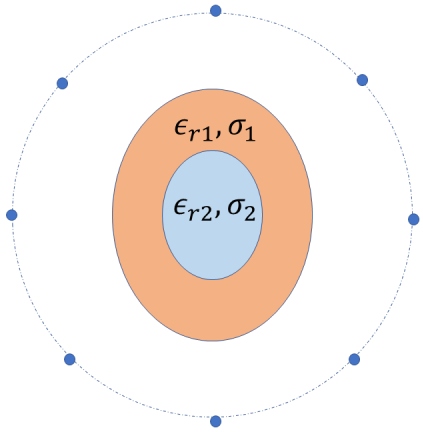

Figure 1.4: A Generic Microwave Diagnosis System [18]

detectable [35]. Significant advancements in this area have been pioneered by our research group at Chalmers University of Technology [18], [36], [37], who have developed multiple generations of a "Strokefinder" device. The latest version of this device, shown in Fig. 1.6, has received CE marking and is ready to support prehospital decision-making [38]. Other research teams around the world have also pursued EM-based stroke detection, reporting promising results in prototype development and unsupervised data analysis [39]–[42].

For ischemic stroke, one of the principal challenges for microwave diagnosis arises from the small size of the occlusive blood clots, which produce only minor permittivity changes that are easily masked by noise or environmental interference. However, the reduced blood volume in the infarction area can also yield detectable permittivity variations [44]. Thus far, most studies on microwave diagnosis of ischemic stroke have focused on simulated data or phantom-based experiments [45]–[47].

A critical clinical objective is to distinguish small vessel occlusions, amenable to thrombolysis, from large vessel occlusions, where thrombectomy can be a verry effective treatment. The hypothesis in this work is that the use of a contrast-enhancing agent (CEA) amplifies the contrast between infarcted and healthy tissue and facilitates discrimination between the types of stroke. Al-

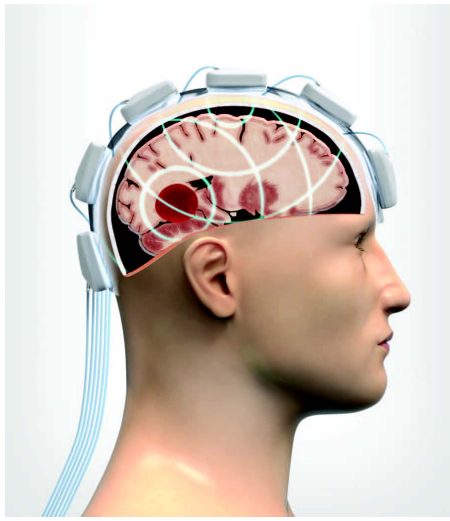

Figure 1.5: A generic sketch of a microwave-based stoke diagnosis system [18]

.

Figure 1.6: The Strokefinder device, MD100, developed by Medfield Diagnostics AB [36], [43]

.

though the use of CEAs in imaging modalities such as MRI has a long history [48], it has also been explored in microwave diagnostics. Some examples include iron nanoparticles [49], zinc oxide nanoparticles [50], superparamagnetic iron oxide nanoparticles [51], and saline solutions [52], with some animal experiments conducted on rabbits [49].

In this work, the main idea is to capitalize on the asymmetry in perfusion that arises when an artery is partially or fully occluded. By introducing a CEA intravenously, the agent travels through the heart and lungs before entering the cerebral circulation, distributing unevenly in the brain when a thrombus impedes blood flow. The hypothesis behind this thesis is that this localized variation in dielectric properties can be detected by the microwave antennas placed around the body, thus offering a potential method to discriminate between healthy and infarcted regions in patients with ischemic stroke.

1.4 Aim of the thesis

The long-term aim of this project is to develop a microwave-based diagnostic system using a contrast enhancement agent to enable the diagnosis of large vessel occlusions in humans. As a first step, this is pursued by designing a specialized antenna system, which, together with the appropriate, developed algorithms, are tested in an animal model. The initial findings of this project were presented in a licentiate thesis earlier [53].

Antenna Design

Operating at lower frequencies is desirable for penetrating deeper into the body's internal organs [28]. However, antennas designed for such low frequencies tend to be physically larger, making it challenging to position them around a patient. To address this, the radiating element in this research is placed inside a medium with high relative permittivity. By doing so, the antenna's physical size is reduced [54]–[57].

In this work the proposal is to move the radiating element of the antenna away from the body surface and inserting a dielectric rod in between. This design confines most of the energy within the rod's core, directing it toward the body rather than allowing it to propagate along its surface. At the same time, the antenna remains well-matched to the body, preserving the ultra-

wideband operation necessary for high-resolution diagnostics [58]. The design is explained thoroughly in paper A.

Animal Model

This research, conducted over several years and involving multiple animals, represents an exploratory study aimed at identifying optimal measurement setups, protocols, and signal processing algorithms. A significant focus was placed on developing a novel animal model for this type of investigation, which has not been previously established. Differences between human and animal vasculature presented challenges that were overcome by testing various experimental protocols, including occlusion location and duration as well as injection dosage and timing of the injections and the measurements. These efforts sought to replicate, first, a scenario in which changes in blood flow can be induced and detected, and second, a scenario involving prolonged occlusion leading to edema formation. In doing so, the study advances the understanding of how to tailor measurement conditions to produce clinically relevant data.

Signal Processing

As a final step toward fulfilling the study's overall objective, various signal processing algorithms were developed to facilitate the analysis and interpretation of measurement data. A simple yet effective pre-processing method was first introduced to detect deviations in the measured microwave transmission signal after the occlusion and injection from the baseline measurements. However, the complexity of the problem—compounded by multiple concurrent physiological effects following a large vessel occlusion—necessitated an advanced technique to disentangle these overlapping influences. Additionally, the lack of abundant measurement data limited the practical use of machine learning approaches. Consequently, physics-based signal detection methods were designed, explored, and tested, ultimately providing the final diagnostic results.

1.5 Thesis outline

The rest of the thesis is structured in the following way: In Chapter 2 the antenna is presented in addition to some supplementary material about the details of the antenna design not included in any publication. Chapter 3 reports on the principles for the animal study, also described in paper F. In Chapter 4, the signal processing algorithms used to detect both the occlusion and contrast agent injection are introduced, following the descriptions in papers D and E. Chapter 5 discusses possible interpretations of the physiological phenomena triggered by stroke and based on the microwave measurements and analysis as discussed in paper F. Chapter 6 summarizes the appended papers, and Chapter 7 concludes the thesis.

CHAPTER 2

Antenna Design

Antennas are important elements in microwave biomedical diagnostics. A well-designed antenna is a critical enabler of accurate diagnostics, while an antenna with poor performance most likely will deteriorate the diagnostic performance. Over the past few years, considerable efforts had been made to design and optimize antennas for a wide range of biomedical diagnostics; some examples include [58]–[68].

Several factors need to be considered in designing an antenna for biomedical diagnostics applications. To list a few:

- **Bandwidth:** The bandwidth of an antenna is characterized by the range of the frequencies where the reflection coefficient of the antenna falls below -10 dB. In this work, the goal is to have an ultra-wideband antenna with a fractional bandwidth of at least 20% that can operate at a large range of frequencies around 1 GHz and enables high-resolution diagnostics [66].

- **Operating frequency:** As the attenuation of the microwaves inside a lossy environment like biological tissues increases with the frequency of the signal, it is desirable to operate at lower frequencies to ensure

enough penetration of the wave to internal organs [28].

- **Compactness:** In a microwave-based biomedical diagnosis system several antennas are commonly placed around the body [63], [67]. Therefore, the antenna's physical size should be small enough so an array of them could be placed on the target organ.

- **Interference Susceptibility:** One problem of on-body antennas is the existence of surface or creeping waves [69]. A part of the radiated wave travels on the surface of the body and is then received by the adjacent antennas, interfering with the direct-path wave and deteriorating the diagnosis accuracy [70]. Therefore, it is advantageous to mitigate these multi-path signals.

It's challenging to design an antenna that possesses all the features mentioned above as attaining one can result in losing the other. For example, an antenna that operates at low frequencies is physically larger than an antenna operating at higher frequencies; therefore, it hinders compactness. Additionally, reaching a wide bandwidth at low frequencies is challenging [71]. Overall, the aim is to develop a compact, wide-band antenna operating below 1 GHz with low interference that can be arranged in an array configuration on the body.

To overcome the aforementioned challenges and meet the goals, the idea is to base the design on a self-grounded bow-tie antenna (SGBTA) [56]. This type of antenna has the advantage of being a wide-band equivalent of the dipoles [72] and is therefore quite popular in different biomedical applications [61], [65], [73]. To improve the performance of SGBTA in terms of matching to the body and reducing the surface wave a, it is turned into a dielectric rod antenna (DRA). The DRA is composed of an SGBTA an its radiating element that is connected to a two-layer dielectric rod. The fundamental design idea behind this antenna is to move the radiating element away from and to guide the radiated wave towards the body by using the dielectric rod in order to minimize surface waves. It is shown that the proposed new antenna design gives a wider bandwidth, stable near-field gain, and a more confined distribution of the power on the surface of the body compared to the SGBTA [74]. The design of this antenna is discussed in detail in the following section and paper A and B in the appendix.

2.1 Dielectric Rod Antenna Design

In this section, the design of the DRA is introduced. This design is based partly based on a 2-dimensional analytical solution to the wave propagation problem in a 2-layers cylindrical structure as shown in Fig. 2.1. This structure consists of a cylindrical core (blue) and cladding (gray) and is aligned with the z-axis. Parameters a and b are the radii and ϵ_{r1} and ϵ_{r2} are the relative permittivities of the core and the cladding respectively. In this analysis, lossless materials are considered with $\epsilon_{r1} = 80$ and $\epsilon_{r2} = 2$ which are close to the permittivity of water and plastic respectively. The surrounding medium is set to be vacuum $\epsilon_{r3} = 1$. According to conclusions in [75], in order to only excite the fundamental mode of the DRA, the radius of the DRA should satisfy the condition $2a < \frac{0.626}{\sqrt{\epsilon_{r1}}}\lambda_0$, where λ_0 is the wavelength in vacuum. If 700 MHz is considered, which is among the frequency range of interest (below 1 GHz) and $\epsilon_r = 80$, the radius a should be smaller than 1.5 cm. On the other hand, to have the field confined to the core, the diameter should be larger than $\frac{\lambda_0}{4}$ [75], resulting in $a > 5.3$ cm. This is in contradiction with the first condition on a and the rule of thumb conditions that were mainly derived for antennas operating at higher frequencies can not be applied here. Instead, a more precise study is needed to evaluate the mode of excitation and field confinement in the DRA in order to suggest an optimal design for the LVO detection application. Therefore, an analytical solution to the wave propagation in an infinite 2D cylindrical structure is presented with emphasis put on the radius of the core of the dielectric rod, as it plays an essential role in the wave propagation in this structure. The field is not confined to the surface of the rod if the core radius is too small while a larger core radius may lead to the excitation of higher, unwanted modes. As a compromise, the value of the core radius is chosen in a way that the fields are confined in the rod and a higher-order mode is excited. Then a mode suppressor is designed to suppress that mode. A mode suppressor is an structure that increases the cut-off frequency of the unwanted higher-order modes. This analysis is presented in paper A. Finally, in order to confirm the design, numerical 3D simulations and experimental measurements are presented in paper A. The connection between the 2D analysis and 3D numerical simulations is investigated in paper B.

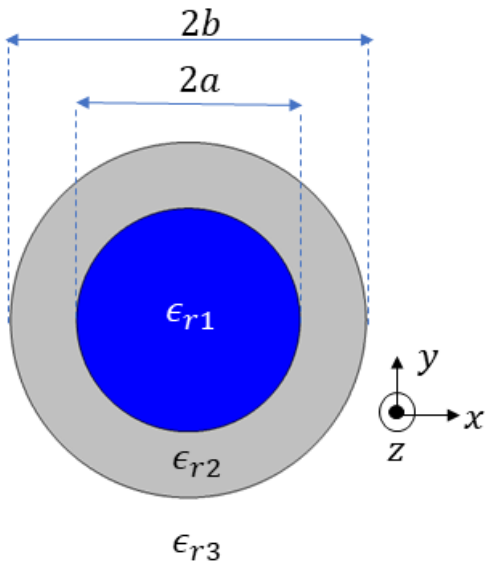

Figure 2.1: The 2D dielectric rod structure

Analytical Solution for a 2 layers DRA

To go in to some more detail on the dielectric rod antenna design, first, the wave propagation in this structure is investigated. Here, the main principles of the analytical solution inside a 2-layer DRA are discussed, together with a derivation of the solution. The first step of the antenna design process is to describe the wave propagation in this structure. This includes a quantitative description of the effects of each of the design parameters (radius of the core and cladding and the permittivity of the core and cladding material) on the wave confinement. The 2-dimensional cylindrical structure considered here is shown in Fig. 2.1.

In [76], an analytical solution to the wave propagation problem was presented. According to the separation of variables technique [77], the solutions to the homogeneous wave equation are found and denoted by the modes of the structure. The axial component (along the rod) of the electric and magnetic

fields of these modes can, according to [76] be written:

$$\begin{aligned} E_{z1} &= A_{n1} Z_{n1}(k_1 r) P_n \quad 0 \leq r \leq a \\ H_{z1} &= B_{n1} Z_{n1}(k_1 r) Q_n \quad 0 \leq r \leq a \end{aligned} \tag{2.1}$$

$$\begin{aligned} E_{z2} &= [A_{n2} Z_{n2}(k_2 r) + A_{n3} Z_{n3}](k_2 r)] P_n \quad a \leq r \leq b \\ H_{z2} &= [B_{n2} Z_{n2}(k_2 r) + B_{n3} Z_{n3}](k_2 r)] Q_n \quad a \leq r \leq b \end{aligned} \tag{2.2}$$

$$\begin{aligned} E_{z3} &= A_{n4} Z_{n4}(k_3 r) P_n \quad b \leq r \\ H_{z3} &= B_{n4} Z_{n4}(k_3 r) Q_n \quad b \leq r \end{aligned} \tag{2.3}$$

where $P_n = \cos(n\phi)\exp(-j\beta z)$ and $Q_n = \sin(n\phi)\exp(-j\beta z)$. The parameter n determines the first mode number and $k_i, \quad i = 1-3$ is the wavenumber in the radial direction. The functions $Z_{nj}, \quad j = 1-4$ are Bessel and modified Bessel functions. The modes in this structure are classified based on where they start to attenuate in the radial direction into two groups. First, the cladding modes are the modes that are attenuated only outside the cladding. The second type of mode is the core mode, where the wave attenuation starts right after the boundary between the core and the cladding. An observation is that attenuation in layer i requires k_i to be imaginary. An alternative way of formulating the field equations is to keep all the equations and variables real and choose the appropriate Bessel function based on in which layer attenuation is desired. A reason for working only with real variables is that it makes the computations less complex and faster. The real-valued k_i is, according to [76], defined as:

$$(k_i)^2 = k_0^2 v_i(\epsilon_{ri}\mu_{ri} - \bar{\beta}^2) \tag{2.4}$$

where $k_0 = \omega\sqrt{\epsilon_0\mu_0}$ is the wave number in vacuum. The parameter v_i is a variable to keep k_i real and controls which Bessel function to choose and is defined as follows:

$$v_i = \begin{cases} 1, & \mu_{ri}\epsilon_{ri} \geq \bar{\beta}^2 \\ -1, & \mu_{ri}\epsilon_{ri} \leq \bar{\beta}^2 \end{cases} \tag{2.5}$$

where $\bar{\beta} = \frac{\beta}{k_0}$ and $i = 1-3$. The equality condition in the definition of v_i is not important, as in this case $k_i = 0$. The choice of Z_{nj} in the above equations determines the type of the mode. For the cladding modes $v_1 = v_2 = 1 \quad \text{and} \quad v_3 = -1$. For these modes $\sqrt{\epsilon_{r3}} \leq \bar{\beta} \leq \sqrt{\epsilon_{r2}}$ considering $\mu_i = 1$ for all layers. For the core modes $v_1 = 1$ and $v_2 = v_3 = -1$. These modes have

$\sqrt{\epsilon_{r2}} \leq \bar{\beta} \leq \sqrt{\epsilon_{r1}}$. From Maxwell's equations, The r and ϕ components can be found. According to the boundary conditions, the tangential components of the electric and magnetic fields are continuous at the boundaries. The continuity of E_z, H_z, E_ϕ and H_ϕ at $r = a$ gives 4 equations. The same field components are continuous at $r = b$, which also provides 4 equations. These 8 equations alongside the 8 unknowns ($A_{nj}, B_{nj} \quad j = 1 - 4$) make an 8 by 8 homogeneous linear system of equations.

$$D_{8\times8}C_{8\times1} = 0 \tag{2.6}$$

where $D_{8\times8}$ is defined as:

$$D_{8\times8} = \begin{bmatrix} Z_{n1}(k_1a) & 0 & -Z_{n2}(k_2a) & -Z_{n3}(k_2a) & \dots \\ 0 & Z_{n1}(k_1a) & 0 & 0 & \dots \\ \frac{n}{ak_1^2}\beta Z_{n1}(k_1a) & \frac{\omega\mu_0}{k_1}Z'_{n1}(k_1a) & \frac{n}{ak_2^2}\beta Z_{n2}(k_2a) & \frac{n}{ak_2^2}\beta Z_{n3}(k_2a) & \dots \\ \frac{\omega\epsilon_0\epsilon_{r1}}{k_1}Z'_{n1}(k_1a) & \frac{n}{ak_1^2}\beta Z_{n1}(k_1a) & \frac{\omega\epsilon_0\epsilon_{r2}}{k_2}Z'_{n2}(k_2a) & \frac{\omega\epsilon_0\epsilon_{r2}}{k_2}Z'_{n3}(k_2a) & \dots \\ 0 & 0 & Z_{n2}(k_2b) & Z_{n3}(k_2b) & \dots \\ 0 & 0 & 0 & 0 & \dots \\ 0 & 0 & -\frac{n}{bk_2^2}\beta Z_{n2}(k_2a) & -\frac{n}{bk_2^2}\beta Z_{n3}(k_2b) & \dots \\ 0 & 0 & \frac{\omega\epsilon_0\epsilon_{r2}}{k_2}Z'_{n2}(k_2b) & \frac{\omega\epsilon_0\epsilon_{r2}}{k_2}Z'_{n3}(k_2b) & \dots \end{bmatrix}$$

$$\begin{bmatrix} \dots & 0 & 0 & 0 & 0 \\ \dots & -Z_{n2}(k_2a) & -Z_{n3}(k_2a) & 0 & 0 \\ \dots & \frac{\omega\mu_0}{k_2}Z'_{n2}(k_2a) & \frac{\omega\mu_0}{k_2}Z'_{n3}(k_2a) & 0 & 0 \\ \dots & \frac{n}{ak_2^2}\beta Z_{n2}(k_2a) & \frac{n}{ak_2^2}\beta Z_{n3}(k_2a) & 0 & 0 \\ \dots & 0 & 0 & -Z_{n4}(k_3b) & 0 \\ \dots & Z_{n2}(k_2b) & Z_{n3}(k_2b) & 0 & -Z_{n4}(k_3b) \\ \dots & -\frac{\omega\mu_0}{k_2}Z'_{n2}(k_2b) & -\frac{\omega\mu_0}{k_2}Z'_{n3}(k_2b) & \frac{n}{bk_3^2}\beta Z_{n4}(k_3b) & \frac{\omega\mu_0}{k_3}Z'_{n4}(k_3b) \\ \dots & \frac{n}{bk_2^2}\beta Z_{n2}(k_2b) & \frac{n}{bk_2^2}\beta Z_{n3}(k_2b) & -\frac{\omega\epsilon_0\epsilon_{r3}}{k_3}Z'_{n4}(k_3b) & -\frac{n}{bk_3^2}\beta Z_{n4}(k_3b) \end{bmatrix} \tag{2.7}$$

Here $(Z_{nj})' = \frac{\partial}{\partial(k_i r)}(Z_{nj})$ and the definition of the function Z_{nj} is given in the table below [76]:

Table 2.1: Definition of the function Z_{nj}

	Z_{n1}		Z_{n2}		Z_{n3}		Z_{n4}
IF	v_1=1	v_1=-1	v_2=1	v_2=-1	v_2=1	v_2=-1	v_3=-1
=	J_n	I_n	J_n	I_n	Y_n	K_n	K_n

J_n and Y_n are the Bessel functions of the first and second kinds respectively. I_n and K_n are the modified Bessel functions of the first and second kind respectively. The appropriate function should be picked based on the type of mode (cladding or core) that is determined by the values for v_1 and v_2. The only nontrivial solution to this system of equations can be obtained by setting the determinant of $D_{8\times 8}$ equal to zero.

$$\det(D_{8\times 8}) = F(\beta) = 0. \tag{2.8}$$

This equation is called the characteristics equation of the structure. Solving the characteristic equation for β yields the dispersion curves of the structure which show the variations of β versus a, the core radius, or frequency. The solution to this equation is explained in detail in paper A.

In order to find the fields' coefficients $C_{8\times 1}$, equation (2.8) should first be solved for β. As the determinant of the $D_{8\times 8}$ is zero, then the the rank of $D_{8\times 8}$ is less than 8 and solving 2.6 is the same as finding the Null Space of $D_{8\times 8}$ [78]. There are several ways to find the Null Space of a matrix. One way is to find the normalized coefficients [79]. The first coefficient, A_{n1} is set to 1 and the other coefficients are found normalized to that. if $A_{n1} = 1$ then the first column of $D_{8\times 8}$ is named $H_{8\times 1}$ and the rest of the columns form matrix $D'_{8\times 7}$. Then the remaining seven coefficients, $G_{7\times 1}$ can be found by solving the following equation:

$$D'_{8\times 7}G_{7\times 1} \quad = \quad -H_{8\times 1} \tag{2.9}$$

This equation is solved for $G_{1\times 7}$ using the function `mldivide` in MATLAB R2020B which finds the solution that satisfies the leas-square error condition [80]. Then, the full coefficient's matrix is:

$$C_{8\times 1} \quad = \quad [1, G^T_{7\times 1}]^T. \tag{2.10}$$

Another method to find the null space is by using singular value decomposition (SVD) which results in the same coefficients as the normalization method.

With the coefficients calculated, the normalized field components for any mode at every location in space can be obtained. The normalized amplitudes of the z-component $|E_z|$ of HE_{11} and (TM_{01}, are plotted in Fig. 2.2. The two vertical dashed lines from left to right show the boundary of the core and cladding respectively. It can be seen that while the cladding mode (TM_{01} at 700 MHz) exhibits an ascending behavior in the cladding and then gets attenuated outside, for the core modes (The other three curves shown in Fig .2.2), the attenuation starts right after the boundary between the core and cladding. This means that the core modes are more confined inside the core, rather than outside it. Therefore, from the confinement point of view, it is more desirable to have a rod with a larger radius. The choice of the radius is investigated in paper A, part II by calculating the normalized modal radius (NMR).

2D Numerical Simulations

To verify the accuracy of the solution presented earlier, the wave propagation problem in this structure is studied by using a 2D numerical solver. This solver is also used to design a mode suppressor that is added to the structure to prevent the excitation of the higher-order modes. For this purpose, the modal analysis study for electromagnetic wave frequency (ewfd) in COMSOL Multiphysics 5.6 is used. In order to find the core and cladding modes, respectively, two different simulations were run. For the former, the solver finds $\bar{\beta}$, around $\sqrt{\epsilon_{r1}}$ while for the latter the search for $\bar{\beta}$ is done around $\sqrt{\epsilon_{r2}}$. In Fig. 2.3, the analytical and numerical dispersion curves are compared with each other. The cladding mode simulation returns only a single propagating mode, but as can be seen in this figure by following the trajectory of the triangles, it is in fact three different modes at different frequencies. A good agreement is seen between the analytical solution and simulation for the core modes at frequencies higher than the cut-off of the core modes which is the frequency where the cladding mode of a type turns into the core mode of the same type, shown by the intersection of the horizontal line at $\sqrt{2}$ with the dispersion curves in this figure. Around these frequencies, some gaps are seen in the numerical dispersion curves, which can be solved by trying different values for n_{eff} which the solver asks to search around. Since we have the

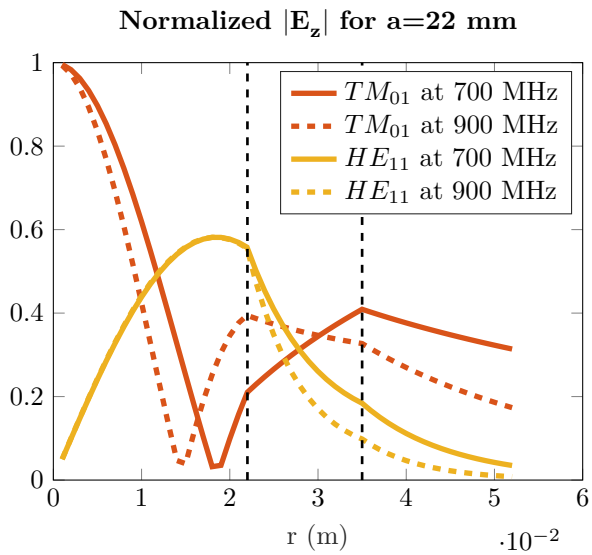

Figure 2.2: Normalized z-component of the electric field for four modes (two core and two cladding modes) at 2 frequencies

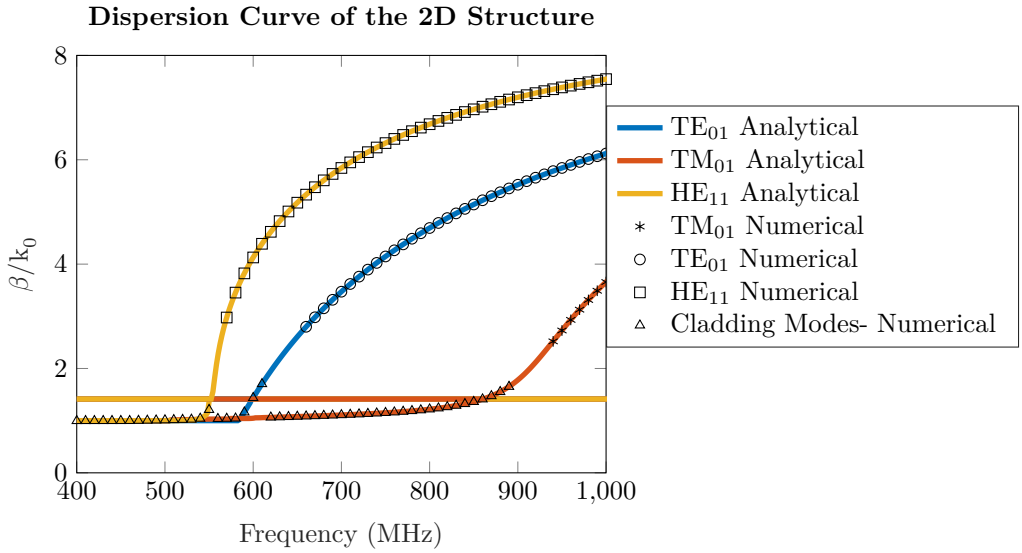

Figure 2.3: Comparison between the analytical and the numerical solutions

exact analytical solution, this approach was not followed.

The magnitude of the electric field for these three modes are shown in Fig. 2.4 at a frequency where they are cladding modes (540 MHz for HE_{11} and 600 MHz for the other two) and core modes (900 MHz for all three modes). In each figure, the cladding and the core modes are shown in the left and right images respectively. Each mode is normalized to its maximum value. The arrows show the direction of the tangential component of the field. From this figure, it can be seen that all of the modes become more confined inside the rod as the mode turns into a core mode.

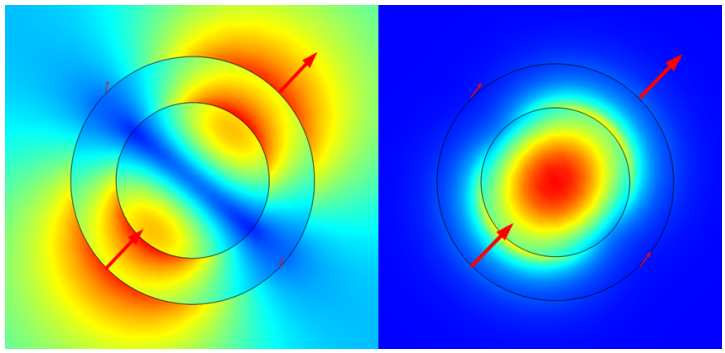

(a) HE_{11} mode

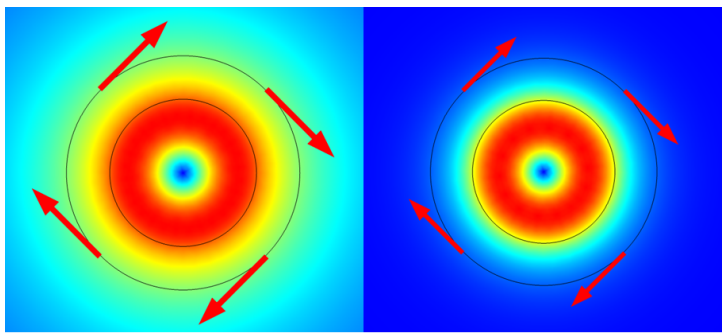

(b) TE_{01} mode

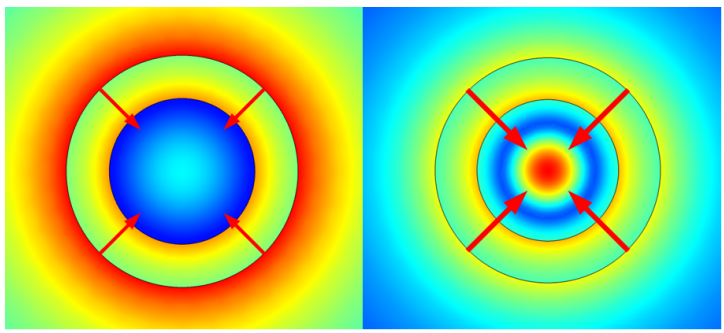

(c) TM_{01} mode

Figure 2.4: The magnitude of the 2D simulated electric fields when they are a cladding (left) and a core (right) mode. The arrows show the direction of the tangential component of the field.

2.2 Launching Efficiency of the 2D Modes in the 3D Structure

The purpose of DRA design was to confine and guide the waves toward the body and prevent their propagation on the body's surface. The design utilizes a solution to the wave equation in a 2D structure and a 2D numerical simulation to design the mode suppressor. For comparison, the accuracy of this modeling was investigated to study how much of the input power that was fed into a 3D structure that is guided through each of these 2D modes. A quantity that measures this proportion is called the launching efficiency, and the way to calculate it is as follows:

First, to show quantitatively how much the higher order modesTE_{01} and TM_{01} are excited, the fields excited on a DRA are written as [81]:

$$E^{3D} = \sum_{p=1}^{m} A_p E_p^{2D} + E_R, \tag{2.11}$$

where E^{3D} is the total 3D field, E_p^{2D} is a 2D guided wave mode, m is the number of the propagating modes, and E_R is the radiating field, i.e. has an imaginary k_3. The unknown of this equation, A_p can be obtained by applying the orthogonality of the guided fields to each other and the radiating field [81]:

$$\int (E_p^{2D} \times H_q^{2D}) \cdot \hat{z} da = 0 \; for \; p \neq q. \tag{2.12}$$

$$\int (E_R \times H_q^{2D}) \cdot \hat{z} da = 0. \tag{2.13}$$

Combining (2.11)-(2.13), the coefficient of each mode can be found as:

$$A_p = \frac{\int (E^{3D} \times H_p^{2D}) \cdot \hat{z} da}{\int (E_p^{2D} \times H_p^{2D}) \cdot \hat{z} da}. \tag{2.14}$$

Finally, the launching efficiency is calculated for a single mode or the summation of the modes and is defined as [82]:

$$\alpha_p = \frac{\frac{1}{2} \int (\Re(\hat{E_p}^{3D} \times \hat{H_p}^{3D^*})) \cdot \hat{z} da}{P_{in}}. \tag{2.15}$$

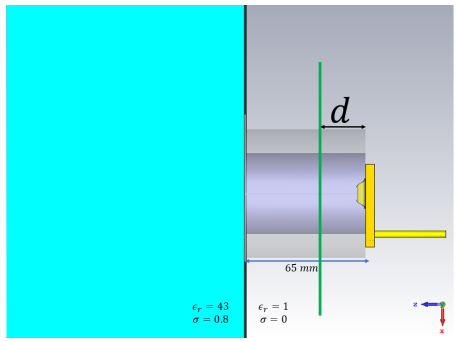

Figure 2.5: The 3D simulated DRA, the sampling plane, is shown with a green line. The Sampling plane is in distance d from the start point of the DRA

Here $*$ denotes the complex conjugate operation, $\hat{E_p}^{3D} = A_p E_p^{2D}$ and $\hat{H_p}^{3D^*}$ are the approximated 3D electric and magnetic fields of each mode respectively. P_{in} shows the total power entered into the exciting element. Here, it had been set to the value of the accepted power in the waveguide port in the 3D simulation to eliminate the effect of the variation in the performance of the exciting element at different frequencies.

The simulation setup is shown in Fig. 2.5 where d is the distance from the start point of the DRA. The launching efficiency, α_p, of each mode is shown in Fig. 2.6 versus d. As seen in this figure, the efficiency of the excitation of the fundamental mode, HE_{11} is considerably higher than that of the two higher-order modes, and it is maintained along the rod. Therefore, the power that is coupled to the higher-order modes is small. To improve this, a mode suppressor is designed in paper A to prevent the excitation of TE_{01}.

2.3 Chapter Summary and Conclusions

In this chapter a novel dielectric rod antenna (DRA) featuring a self-frounded bow-tie antenna (SGBTA) paired with a two-layer dielectric rod. This design reduces surface wave interference up to 10 dB and increases and the bandwidth by 72% compared with SGBTA as shown in paper A. This antenna operates in the frequency band 600- 1500 MHz and has a dimension of

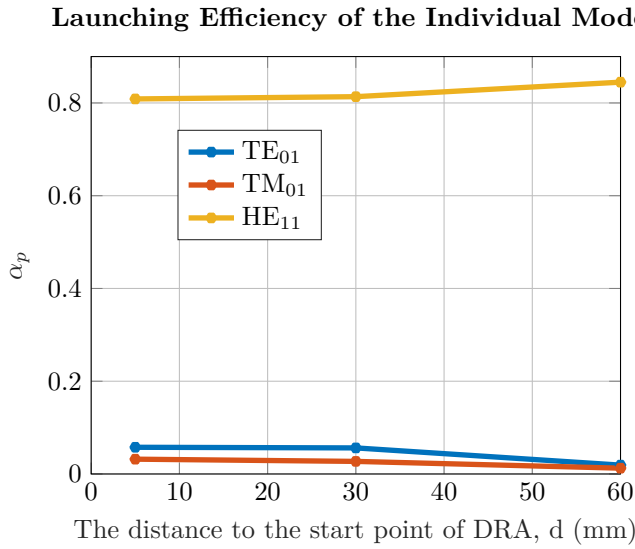

Figure 2.6: Launching efficiency of each mode versus the distance of the sampling plane to the start point of the DRA, d.

$0.15 \times 0.15 \times 0.13\lambda_0$ which equals to $7 \times 7 \times 6.5$ cm. Thus, an array of this antenna could be fit on the patient's head Analytical studies and simulations explore wave propagation in the DRA's cylindrical structure, revealing how core radius influences mode excitation and field confinement. Numerical and experimental validations confirm that the design effectively confines fields, prioritizes the fundamental mode, and suppresses unwanted higher-order modes. This innovative approach in antenna design for biomedical detection results in a robust, high-performing antenna tailored to meet the complex demands of this field.

CHAPTER 3

Animal Study

This chapter summarizes the animal studies. The aim of the animal study is to show the feasibility of microwave detection of the large vessel occlusion. Toward that aim, the following step needs to be taken:

- Finding the occlusion location and duration in sheep to mimic a human LVO as closely as possible.
- Finding the optimal injection dosage to create detectable asymmetry while still being safe for the animal and subsequently for the patient.
- Test the developed microwave detection setup based on the designed antennas that were introduced in Chapter 2.

3.1 The Necessity and Conditions of the Animal Study

The dielectric contrast in the brain during an ischemic stroke is substantially small, making analyzing microwave measurements challenging and introducing notable uncertainties in detection accuracy. Although a novel antenna design

was proposed in Chapter 2 to enhance measurement performance, this innovation alone is insufficient—especially given the lack of pre-stroke baseline measurements. The central idea of this thesis is to magnify the dielectric changes associated with ischemic stroke using a contrast-enhancing agent (CEA) in the form of saline. Consequently, the detection procedure becomes invasive. Although physiological saline solutions are already standard in healthcare, they have not been applied to stroke detection. It is therefore essential to evaluate this method in an animal study before considering clinical tests on humans. Several studies have explored using pigs [44] and rabbits [49], [83], [84] for microwave-based stroke detection. However, pigs present a relatively small brain volume compared to their total head volume, while rabbits have a head size that is significantly smaller than a human's, making any shared instrumentation between these species and humans impractical. Consequently, sheep as a large non-primate animal model were selected for this study due to their head dimensions, which are more comparable to human proportions [85], and their larger brain volume compared to pigs. This choice allows for a more direct adaptation of the developed measurement system to human applications. The use of sheep in translational stroke research as a large animal model is well established [86], [87].

The animal study is performed at the SEARCH laboratory of the Faculty of Veterinary Medicine, Norwegian University of Life Sciences, Sandnes, Norway. In what follows, the regulations on the use of animals in research are reviewed.

The Use of Animals in Research

In Norway, the use of laboratory animals is governed by the regulation concerning the use of animals for scientific purposes (FOR-2015-06-18-761) [88] with one amendment [89]. Furthermore, the National Committee for Research Ethics in Science and Technology (NENT) has published a set of ethical guidelines [90]. According to them, the ethical grounds for the moral duties regarding the animals are based on the following three principles:

- Animals have intrinsic value that must be respected.
- Animals are sentient creatures with the capacity to feel pain, and the interests of animals must be taken into consideration.
- Our treatment of animals is an expression of our attitudes as moral actors.

This guideline further states 10 responsibilities and requirements when animals are used in research. Among them, the three Rs (Replace, Reduce, and Refine) are emphasized here. The remaining 7 are based on them. The three Rs are:

- **Replace**: Researchers are responsible for studying whether it is possible to replace animals with other alternatives. In the research project presented in this thesis, as much development as possible is made based on computer simulations and tests on tissue-mimicking phantoms. Ultimately, animal tests are inevitable. The detection method fundamentally requires an understanding of the saline solution and its behavior in the blood circulatory system. However, by using. computer simulations and phantom experiments, the next R is also addressed, which is:

- **Reduce**: Researchers are responsible for considering if the number of animals could be reduced. In the research project presented in this thesis, the strategy has been that in case of clear results indicating success or failure, the experiments on animals should be stopped and no more animals shall suffer.

- **Refine**: Researchers are responsible for minimizing the risk of suffering for the animals. In this project, all work concerning the welfare of the animal was performed by veterinarians and all experiments we made on anesthetized animals.

Ethical Approval

The ethical approval for the animal experiments is given by the Norwegian Food Safety Authority [91], [92]. All animal housing and experiments were conducted in strict accordance with the guidelines. The ewes were properly sedated prior to initiating anesthesia. Then, they were anesthetized adequately and monitored continuously. Their vital signs, including systolic and diastolic blood pressure, heart rate, SpO_2, and core body temperature, were monitored continuously during the experiment. The animals were euthanized while still anesthetized.

3.2 Procedures for Animal Study

The LVO stroke scenario was studied in a sheep model by occluding the arteries on the left side of the sheep's brain. This is potentially causing an asymmetry in blood flow, which manifests itself as a small asymmetry in microwave attenuation between the occluded and non-occluded sides of the brain. The injection of saline solution will further amplify the asymmetry between the occluded and non-occluded sides.

In addition, the saline solution might also affect the edema formation caused by the occlusion [93].

Next, the experimental setup for the animal measurement is described, including the occlusion locations and durations. Then the measurement protocols are described, specific to both short and long occlusion scenarios, detailing the timing and procedure of each. Following this, a brief description of the detection algorithms is provided. Finally, a description of the processing of the CT scans for analyzing the edema formation.

Occlusion location and duration

In humans, the primary arteries supplying cerebral blood flow are the left and right Common Carotid Arteries (CCA), originating from the aortic arch and brachiocephalic trunk, respectively. These arteries bifurcate into internal and external carotid arteries in the neck. The external carotid arteries (ECA) supply blood to the face and neck, while the internal carotid arteries deliver blood to the brain. An additional pathway to the brain is provided by the left and right vertebral arteries (VA), which merge to form the basilar artery. These arteries are interconnected via the Circle of Willis, facilitating the possibility for collateral blood flow between the two hemispheres of the brain. This vascular anatomy is illustrated in Fig. 3.2.

Sheep share a similar cerebral blood supply system but with two notable differences. First, sheep lack a direct bifurcation of CCA to ICA and ECA. Instead, the ECA connects to a dense network of arteries called the Rete Mirabile (RM), which further connects into the ICA and then the Circle of Willis. This anatomical feature restricts the ability to block higher-up arteries using intra-arterial catheter occlusion [94]. Second, there is a connection between the CCA and VA before reaching the Circle of Willis, as shown by the CVA in Fig. 3.2. To effectively block blood flow to one hemisphere of the

brain, there are three options of occlusion location in sheep [95], as is shown using three colors in Fig. 3.1. In this figure, the red lines show the occlusion of both CCA and occipital artery, blue shows the occluding of both CCA and VA, and green demonstrates the occlusion of ECA. Blocking only one artery results in partial occlusion.

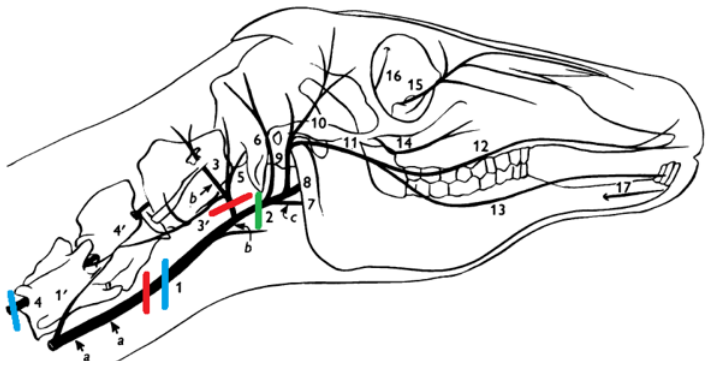

Figure 3.1: The main arteries of the head and neck: 1. common carotid artery (CCA); 2. external carotid artery (ECA); 3. occipital artery (OA); and 4. vertebral artery (VA). The three options of occlusion location in sheep are shown in three colors, red: occluding both CCA and OA, blue: occluding both CCA and VA, and green: occluding ECA. Picture from [96].

The proposed detection method was tested on two animals when blood supply was blocked by occluding blood vessels: one animal with occlusion of both arteries and one with only a single artery occluded. The measurements were analyzed in order to detect the occlusion event. Comparison of the results from the twp occlusion strategies highlights the differences between the sheep's and the human's vessel structure.

This method of occlusion is essential to creating a controlled ischemic environment for this study, allowing for the assessment of the microwave-based detection method under conditions that are similar to those induced by large-vessel occlusions in humans. Two types of occlusions have been investigated: long occlusions and short occlusions. The details of the occlusion location for each cycle are given in subsections 3.2 and 3.2.

The purpose of the short occlusion is to induce a temporary asymmetry in

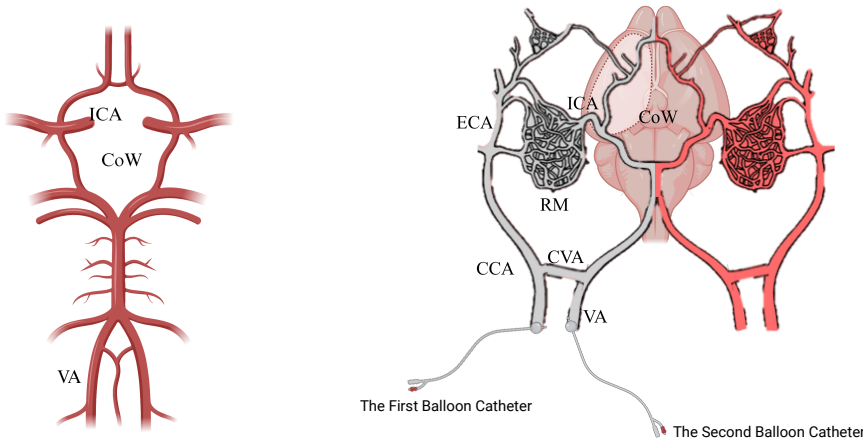

Figure 3.2: Schematic view of the cerebral arteries in humans (left) and sheep (right). CCA: Common Carotid Artery, VA: vertebral Artery, CVA: Carotid-Vertebral-Anastomosis, ICA: Internal Carotid Artery, ECA: External Carotid Artery, RM: Rete Mirabile, CoW: Circle of Willi's. The occlusion locations are shown with two balloon catheters. The sheep's arterial structure is adopted from [97]. The image was created using BioRender.com.

cerebral blood flow within the brief time window before collateral circulation through the Circle of Willis reaches the occluded hemisphere [95]. To test the idea that partially blocked blood flow to the brain can be detected by leveraging the effect of saline on electromagnetic waves, saline is introduced during the occlusion. That further enhances the contrast between the left and right hemispheres, increasing the asymmetry and improving the potential for detection.

The purpose of the long occlusion is to simulate a more clinically relevant scenario with a delay between the stroke onset and the arrival of the ambulance to the suspected stroke patient. Under these conditions, it is expected that the formation of brain edema could have started. This is in accordance with the findings in [98], where a blockage of both the common carotid and vertebral arteries for at least 12 minutes results in observable histological damage in post-mortem brain tissue. This setup enables the investigation of the impact of prolonged ischemia on brain tissue and the observation of any possible subsequent edema development.

Measurement Protocol

In this section, first, the main idea of the measurement protocol is introduced. Then the injection concentration and the details for the short and long occlusions for each animal are described.

The main hypothesis, to be tested in this work, is that the injection of the contrast enhancement agent increases the dielectric asymmetry caused by the asymmetric occlusion of the blood flow. The hypothesis is further that this injection will facilitate increased detection performance of the system. Since the occlusion is done before the Circle of Willi's, it can be anticipated that the collateral flow will bring some contrast agent also to the occluded side. Even if this occurs with some delay, it will potentially reduce the detection performance. Therefore, a simultaneous occlusion and injection were also performed to utilize the time window before the collateral flow evens out the induced asymmetry [95]. In the explored method, this asymmetry is detected using microwave measurements.

Short Occlusions

As already explained, the purpose of the short occlusions is to induce a transient asymmetry in cerebral blood flow, ensuring that the contrast agent reaches its peak concentration before collateral circulation becomes established.

The procedure is performed according to the following steps.

1. Before any measurements begin, the animal is anesthetized and ventilated.

2. The short occlusion measurement protocol starts with a baseline measurement to estimate noise and movement artifacts due to ventilation.

3. The occlusion is induced by inflating the balloon inserted by a catheter into the target arteries. Immediately after completing the occlusion, a saline injection is administered into the jugular vein for animals 1 and 2. For animals 3 and 4, a one-minute delay is introduced between the occlusion and the injection. This enables an investigation of the effects of the injection under collateral flow compensation.

Details regarding the short occlusions and injections are provided in Table 3.1. In the table, the number after A shows the animal number. The letter S indicates a short occlusion. The number after S shows the measurement cycle of that animal.

In all short occlusions, the balloon is deflated to remove the blockage one minute after the injection. In the A2S3 cycle, the injection is administered before the occlusion to serve as a control, allowing for observations of the effect of the injection alone. However, it is important to note that this is the third cycle on that animal, and collateral flow may already have altered from previous cycles.

For animals 1 and 2, long occlusions followed the short occlusions, while for animals 3 and 4, no long occlusions were performed. For animal 5, only the long occlusion was performed.

Long Occlusions

As mentioned earlier, the purpose of the long occlusions is to observe the effects of injection on a model where the stroke onset happened some time ago

and assess its detectability via microwave measurements. Details regarding the long occlusions and injections are provided in Table 3.2.

The protocol is summarized as

1. A baseline measurement to capture the brain's initial state.

2. The occlusion is applied, and measurements are taken for 12 minutes to monitor the progression of ischemia.

3. The saline injection is administered, and measurements continue for another 12 minutes to observe any effects on edema.

This long occlusion procedure was carried out on animals 1 and 2, occluding both the common carotid and vertebral arteries, and on animal 5, occluding only the common carotid artery. The latter is done to investigate the effect of a partially occluded hemisphere.

Injection Concentration

Osmotherapy, e.g. hypertonic therapy, is an effective intervention to manage cerebral edema and reduce elevated intracranial pressure, targeting the underlying mechanisms of edema formation. Injecting hypertonic saline may help to reverse or slow the development of edema by influencing fluid dynamics in brain tissue [99]. Osmotherapy works by creating an osmotic gradient that draws water out of swollen brain tissue and into the bloodstream, thereby dehydrating the tissue [93].

For the short occlusions, it is crucial to obtain a rapid peak in sodium concentration before collateral circulation begins, as this ensures the highest possible asymmetry in dielectric properties between the hemispheres and consequently also in the measured microwave signals. To accomplish this, a small volume of water with a high sodium concentration was injected. Tables 3.1 and 3.2 provide a summary of the injected salt concentrations and the blood sodium levels measured before and after each injection. Results are given for both the short and long occlusions, respectively. For the long occlusion, the saline concentration was the same as for the short occlusions for animals 1 and 2. In animal 5, the effect of a higher salt mass but with a lower concentration was studied.

Table 3.1: Summary of the Short Occlusions

Cycle Code	Injection Dose and Blood Sodium Concentration	Description
A1S1	100 mmol in 25 ml 137 to 148 mmol/L	10 baseline measurements followed by 10 measurements during the simultaneous injection and occlusion (2 arteries) followed by 10 measurements after the termination of occlusion
A2S1	100 mmol in 25 ml 140 to 165 mmol/L	10 baseline measurements followed by 10 measurements during the simultaneous injection and occlusion (1 artery) followed by 10 measurements after the termination of occlusion
A2S2	100 mmol in 25 ml 141 to 164 mmol/L	10 baseline measurements followed by 10 measurements during the simultaneous injection and occlusion (2 arteries) followed by 10 measurements after the termination of occlusion
A2S3	125 mmol in 32 ml 144 to 173 mmol/L	10 baseline measurements followed by 10 measurements during the injection and a delayed occlusion (2 arteries) followed by 10 measurements after the termination of occlusion
A3S1	100 mmol in 25 ml 140 to 148 mmol/L	10 baseline measurements followed by 10 measurements during the occlusion followed by 10 measurements during the injection (1 artery) followed by 10 measurements after the termination of occlusion
A4S1	100 mmol in 25 ml 147 to 164 mmol/L	10 baseline measurement followed by 10 measurements during the occlusion followed by 10 measurements during the injection (1 artery) followed by 10 measurements after the termination of occlusion

Note 1: Here A1 stands for animal 1, and S1 stands for the first short cycle on that animal, and so on.

Table 3.2: Summary of the Long Occlusions

Cycle Code	Injection Dose and Blood Sodium concentration	Description
A1L	100 mmol in 25 ml 140 to 190 mmol/L	10 Baseline measurement followed by 180 measurements during the occlusion (2 arteries) and 154 measurements after the injection
A2L	125 mmol in 32 ml 147 to 170 mmol/L	40 Baseline measurement followed by 180 measurements during the occlusion (2 arteries) and 180 measurements after the injection
A5L	171 mmol in 125 ml No data	15 Baseline measurement followed by 10 measurements during the occlusion (1 artery) and 12 measurements after the injection

Note 1: The number after A shows the animal number. The letter L indicates a long occlusion.
Note 2: For animals 1 and 2 each measurement is 6 seconds while for animal 5, each measurement takes 2.6 minutes.

Microwave Detection Setup

The microwave measurement setup is shown in Fig. 3.3. A 2-port microwave transceiver from Keysight was used for the measurements, operating in the frequency range of 400 to 1200 MHz [100]. For animals 1 through 4, each

measurement took approximately 6 seconds. However, for animal 5, where two transceivers were tested to compare their performance and additional antennas were used, each measurement required 2.6 minutes.

The microwave detection setup included three Dielectric Rod Antennas [74], positioned as follows: one antenna was placed on the forehead, and the remaining two on either side of the head, as shown in the accompanying diagram. The antennas were pointed towards the cortical surface using guidance from CT. The setup also incorporated a switch to toggle between two channels: one channel for the occluded side and the other for the non-occluded, termed the "non-occluded channel." This antenna arrangement is illustrated in Fig. 3.4.

With this setup, each antenna transmits microwave signals into the sheep brain, and the signals received by the other antennas are measured as transmission coefficients. These parameters represent the ratio of the received wave's power to that of the transmitted wave.

Because the reflection from the skin dominates reflection S-parameters, we focus on transmission S-parameters, which provide deeper insights into intracranial conditions.

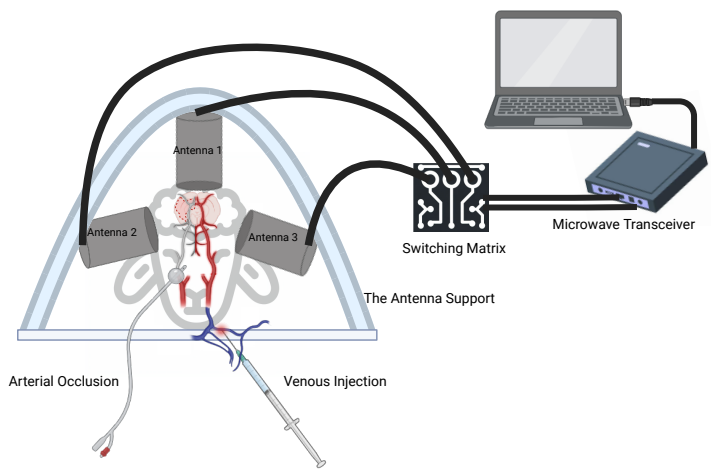

Figure 3.3: Microwave measurement setup. The image was created using BioRender.com.

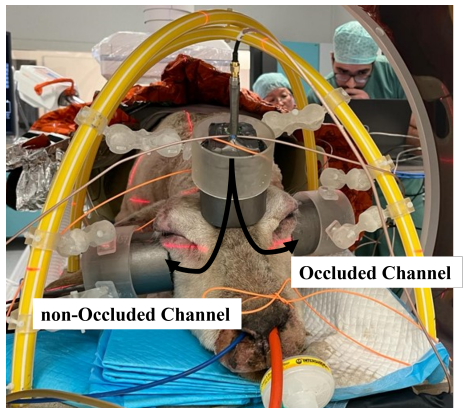

Figure 3.4: non-Occluded and Occluded Channel shown on a sheep.

3.3 Chapter Summary and Conclusions

In this chapter, the animal experiments are detailed and summarized in two tables. Key protocol components—occlusion location, duration, injection concentration, and timing—are presented alongside the purpose and distinctions between short and long occlusions. The measurement setup is also introduced.

Conducted over several years and involving multiple animals, this research represents an exploratory study aimed at determining optimal measurement configurations, protocols, and signal processing approaches. A major emphasis was placed on developing a working protocol for the used animal model tailored to the requirements of this investigation, marking an important step in advancing research in this area.

A limitation of this study is the absence of a control measurement using an independent method (such as CT) to verify the observed asymmetry. Without such external validation, the study must rely solely on microwave measurements, introducing uncertainty about whether the detected asymmetry precisely reflects the underlying physiological changes.

In the next chapter, the signal processing algorithms developed to analyze and interpret the measured microwave signals are introduced, and the main results are presented.

CHAPTER 4

Signal Processing

In this chapter, the developed signal-processing algorithms are introduced. It consists of two parts, first preprocessing and then processing. The first part is introduced in Paper C, and the processing part is in Paper D of this thesis.

4.1 Preprocessing: Detecting a change

The received signal after the occlusion or injection can be summarized with a simple expression in terms of the transmission coefficient between a pair of antennas. The received signal can be viewed as a sum of three components: the baseline, noise, and a change in the signal levels due to occlusion and/or injection. These equations are given in Eq. 4.1.

$$\begin{aligned} X(f) &= X_B(f) + X_A(f) + n(f), \\ \Delta &= X(f) - X_B(f) = X_A(f) + n(f). \end{aligned} \tag{4.1}$$

Here $X_B(f)$ is the baseline, which is the average over 10 transmission signals X_b measured during the baseline phase as, $X_B \simeq \frac{1}{10}\sum_{b=1}^{b=10} X_b$. $X_A(f)$ is

contribution to the transmissions due to the occlusion and injection and $n(f)$ is the frequency-dependent noise. The frequency is represented by f. During the baseline measurement, the only temporal change in the signal is due to the noise and movement artifacts (breathing). Therefore, it is also possible to estimate the power of $n(f) = \sigma(f)$, which is equal to the standard deviation of the 10 baseline measurements. Δ is the differential signal indicating the change in the signal from the baseline caused by the occlusion and injection.

The main purpose of a detection algorithm is to identify significant changes in Δ due to an occlusion or injection. The basis of the algorithm is a comparison of the power of Δ to the noise level, σ at each frequency. If the power exceeds σ, the change is considered a true change; otherwise, it is treated as a false change, i.e., no change in data. In this work, the algorithm's performance is quantified by the ratio of correctly detected changes across frequencies to the total number of frequency points [101]. This algorithm is similar to a Neyman-Pearson detector [102] and here it is named the Signal Power Comparison Algorithm for the Detection of Anomalies (SPCADA). The steps for a signal with N_{all} measured frequencies can be summarized as

Algorithm 1 SPCADA Algorithm

```
N_T = N_F = 0
for i = 1 : N_all do
    if |Δ_i| > σ_i then
        N_T = N_T + 1
    else
        N_F = N_F + 1
```

The detection rate (DR) is defined as the number of detected true changes, N_T divided by the true plus false detection, equal to the number of measured frequencies, $N_{all} = N_T + N_F$.

$$DR = \frac{N_T}{N_{all}} \tag{4.2}$$

Analysis of Differential Signals Across Measurement Phases

The analysis begins by taking the average of the ten measurements during the baseline stage, X_B, and subtracting it from all the measurements of all stages, including the baseline, to find the differential signals. To see if there's

a general trend across the three measurement stages, the average of all the measurements in each stage is shown in Figs. 4.1 and 4.2 for the non-occluded and occluded channels, respectively. The standard deviation among the measurements of each stage is shown by the highlighted areas.

As evident in these figures, it is challenging to draw definitive conclusions about the trends between the injection+occlusion phase and after the reopening of the occlusion as there is significant overlap and similarities across frequencies for both these channels. This overlap could possibly be attributed to the time-dependent nature of the changes being analyzed, where averaging the signals over an entire phase may obscure these temporal variations.

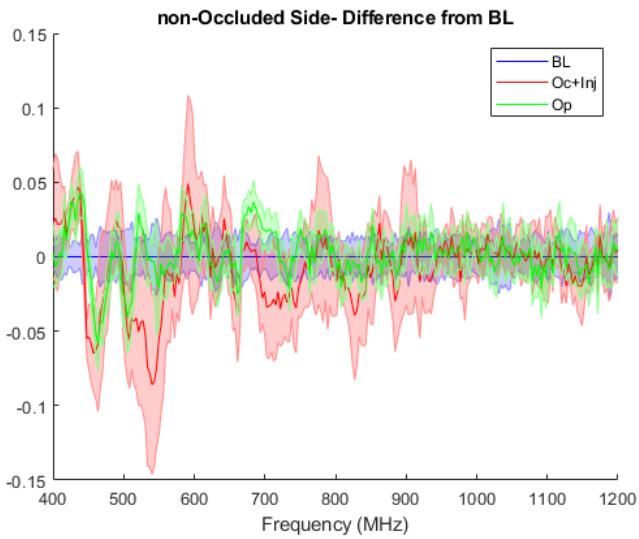

Figure 4.1: The average of the Δ signal of the non-occluded channel of animal 1 in each measurement phase is shown as a solid line, and the standard deviation is shown as the highlighted area. BL: Baseline, Oc+Inj: Simultaneous Occlusion and Injection, Op: Opening

Detection with the SPCADA on measured data

As seen in the previous section, taking the average of all measurements in a measurement phase is not an effective way to conclude how the occlusion and

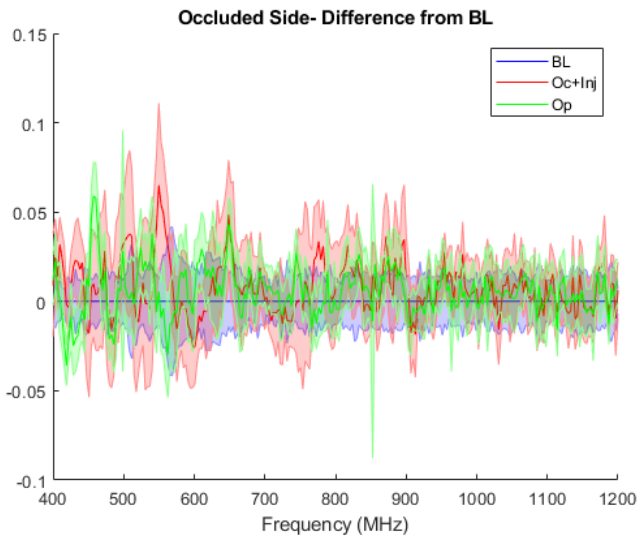

Figure 4.2: The average of the Δ signal of the occluded channel of animal 1 in each measurement phase is shown as a solid line, and the standard deviation is shown as the highlighted area. BL: Baseline, Oc+Inj: Simultaneous Occlusion and Injection, Op: Opening

injection have affected the baseline signals. A single measure is needed that combines the changes that happened across all the frequencies of that measurement. The SPCADA algorithm presented earlier is an elegant way to do this by taking a probabilistic view of the data and revealing what proportions of the measured frequencies demonstrate a change greater than the baseline's noise level. In this section, the results of the testing of the SPCADA algorithm are presented.

The first step in this algorithm is to find the true and false changes. A true change in frequency f is an element of the differential signal, Δ, that its absolute value is higher than the noise power σ at frequency f. Figs. 4.3 and 4.4 illustrate the detectable changes in the non-occluded and occluded channels, respectively. In these figures, the x-axis shows the frequency range, and the y-axis shows the time. The first 10 measurement numbers belong to the baseline phase. The next 10 measurements correspond to the occlusion+injection phase. The last 10 is the opening phase. The horizontal red lines show the separation of each of the phases. The baseline levels were used as a threshold to classify the transmission change as "1-true change", highlighted in yellow squares, and "0-false change", depicted as blue squares. In the figure, it is seen at what measurement number and at what frequency a true change is detected. It is seen that the density of the yellow squares increases between the measurement numbers 11 to 20 (Oc+Inj) compared to 1 to 10 (BL) and 21 to 30 (Op).

The last step in this algorithm is to find a single value for each measurement number that combines the effect of all the frequencies. This is done by calculating the average of each of the rows of these figures. This gives the detection rate (DR) for each measurement number. The detection rates are shown in Fig. 4.5. The vertical lines show the starting moment of each phase of the measurement. In Fig. 4.5 a considerable change in the detection rate can be seen right after the injection and occlusion were completed. As expected, the change has a higher value in the non-occluded channel, capturing the effect of the injection.

The results of the other animals are presented in paper D.

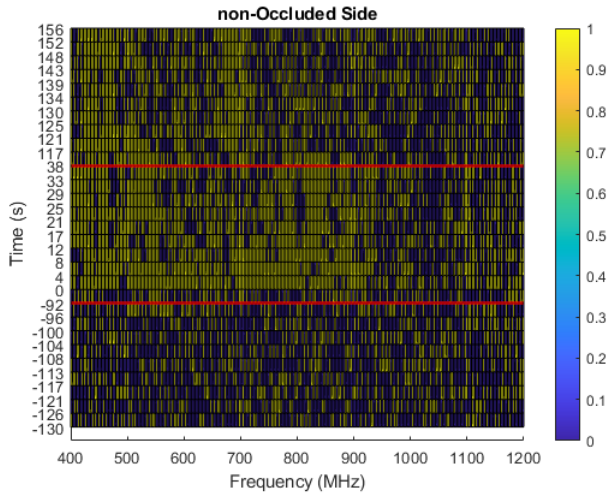

Figure 4.3: True (yellow) and false (blue) changes at each time and each frequency for the channel on the non-occluded side of Animal 1

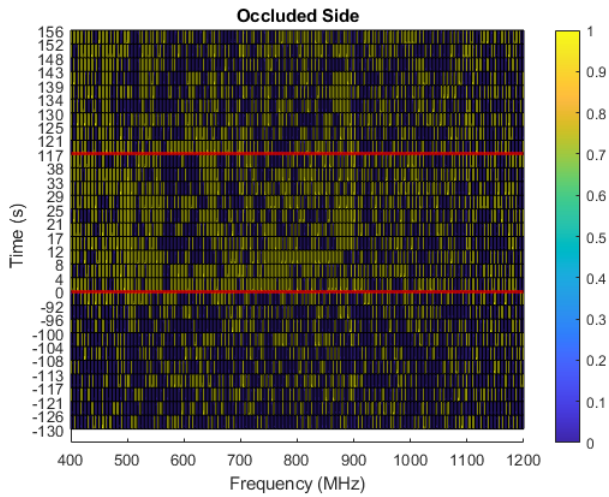

Figure 4.4: True (yellow) and false (blue) changes at each time and each frequency for the channel on the occluded side of Animal 1

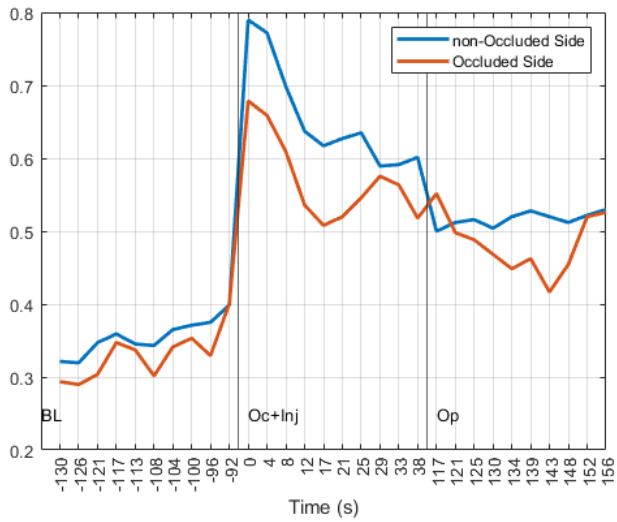

Figure 4.5: Detection Rate for animal 1 across the three phases (BL: baseline, Oc+Inj: occlusion+injection, Op: opening) for the non-occluded channel (blue) and the occluded channel (red).

4.2 Processing: a Physics-Based Frequency Derivative Algorithm

A challenge associated with the measurement protocol of simultaneous injection and occlusion is to separate the effects of the occlusion from the effects of the injection in the microwave data. For stroke detection, we are using the asymmetry caused by the injection as an indication of the stroke. It is therefore important to distinguish the effect of the injection from other effects. The results are most compelling when it is possible to demonstrate that the observed changes are specifically due to the injection and not confounded by the simultaneous occlusion.

To address this problem, a novel algorithm was developed; it was based on both theoretical analysis and numerical simulation study in a 3D sheep's head model. The proposed algorithm is grounded in the underlying physics of the occlusion and injection stages. More specifically, the conductivity of the non-occluded side of the brain is enhanced by saline injection, and this enhancement is frequency-dependent due to the dispersive properties of the saline. It can be shown that this characteristic is represented in the second-order derivative of the measured signal with respect to the frequency. Therefore, based on the sign of the measured differential signal and its second-order derivative, the signal can be classified into four different types. Identification of the type is the core principle of the detection in this algorithm.

The type detection algorithm is based on a theoretical analysis that correlates the measured changes in the microwave signals due to changes in brain conductivity from the occlusion and injection. The algorithm is summarized in a flow chart in Fig. 4.11). When applying the type detection method to experimental data, rapid changes across the frequencies are expected, both changes to the sign of the signal and its second-order derivative. As a first step to cope with these variations, frequency windows of varying widths over the signal are defined. The type detection is applied to each of these windows, and the results are later merged to find the general trend across all measured frequencies.

Subsequently, the algorithm has been tested both on simulated s-parameters in different realistic detection scenarios as well as on measured data on the sheep.

Theoretical analysis

The purpose of the theoretical analysis is to derive a relation between the measured changes in the microwave data and their origin in dielectric changes in the brain caused by occlusion and injection events. Particularly this is made by analyzing dispersive characteristics of the dielectric changes and their implications on the measured data. This relation will then serve as a basis for the type detection algorithm. The analysis is, in this case, restricted to the amplitudes of the microwave data.

Electromagnetically, the animal can be considered as spatially varying complex permittivities, as:

$$\epsilon(\vec{R}) = \Re(\epsilon(\vec{R})) - j\Im(\epsilon(\vec{R})) \tag{4.3}$$

where $\vec{R}$ is the spatial coordinate, $\Re(\epsilon) = \epsilon'$ is the real part of the permittivity, also called the dielectric constant. The dielectric constant can be frequency-dependent. The imaginary part of the permittivity, the loss factor, consists of two parts:

$$\Im(\epsilon) = \epsilon'' + \frac{\sigma}{\omega\epsilon_0} \tag{4.4}$$

where ϵ'' represents a frequency dependent dielectric loss and σ is the DC conductivity.

In the case of a stroke or injection of a contrast agent, the complex permittivity distribution in the brain is changed. These changes are represented by the parameters α and β, which denote the relative changes in the real part (dielectric constant) and imaginary part (loss factor), respectively. The relative change in the dielectric loss, ϵ'' is denoted α''.

The first term in equation 4.11 is related to the real part of the permittivity through Krammers-Kronig relations:

$$\epsilon'(\omega) = \frac{2}{\pi} P \int \frac{X\epsilon''(\omega)}{X^2 - \omega^2} dX + 1 \tag{4.5}$$

Where P stands for the principal value of the integral and X is a dummy variable for frequency. Let's see how much ϵ' will change (shown by α) if ϵ'' is changed by a factor of $1 + \alpha''$.

$$(1 + \alpha)\epsilon'(\omega) = \frac{2}{\pi} P \int \frac{X(1 + \alpha'')\epsilon''(\omega)}{X^2 - \omega^2} dX + 1 \tag{4.6}$$

From above, if α'' is frequency independent, it can be concluded that:

$$1 + \alpha = \frac{1 + (1 + \alpha'')A}{1 + A} \tag{4.7}$$

where

$$A = \frac{2}{\pi} P \int \frac{X\epsilon''(\omega)}{X^2 - \omega^2} dX \tag{4.8}$$

if $A = \epsilon' - 1 >> 1$ then it follows that

$$1 + \alpha \approx \frac{1 + (1 + \alpha'')A}{A} = \frac{1}{A} + (1 + \alpha'') = \frac{1}{\epsilon' - 1} + 1 + \alpha''. \tag{4.9}$$

As mentioned, for most biological tissues like blood and brain, $\epsilon' - 1 >> 1$, therefore $\alpha \approx \alpha''$. This means the changes in the real part of the permittivity and the first term in the imaginary part are the same. The change in the complex permittivity due to occlusion or injection can be different and is modeled by different α and β .

The injection will increase the salinity of the blood, resulting as well as an increase in the conductivity. If this relative change is denoted γ, then the overall change in both the real and imaginary parts of the complex permittivity can be summarized as:

$$\Re(\epsilon_{new}) = (1 + \alpha)\Re(\epsilon) \tag{4.10}$$

$$\Im(\epsilon_{new}) = (1 + \beta)\Im(\epsilon) = (1 + \alpha)\epsilon'' + (1 + \gamma)\frac{\sigma}{\omega\epsilon_0} \tag{4.11}$$

Based on the assumptions, it can be concluded that the injection of saline will lead to $\gamma > 0$ an increase in the charge carrier (ions) in the solution. The increase of ions will also result in a negative α because ions stick to water molecules and reduce their ability to alternate with the external electric field [103]. A quick and easy way to see how a positive γ and negative α will affect β is to use the first-order Debye model for saline [104].

Fig. 4.6 shows the real and imaginary parts of the complex permittivity of a saline solution in the frequency range of interest when the salt concentration is 70 mmol/L and 100 mmol/L, respectively. It can be seen that as the salt concentration increases, the imaginary part increases considerably while the changes in the real part are relatively small. The corresponding relative changes to the dielectric constant (α), DC conductivity (γ), and loss factor(β),

are plotted in Fig. 4.7.

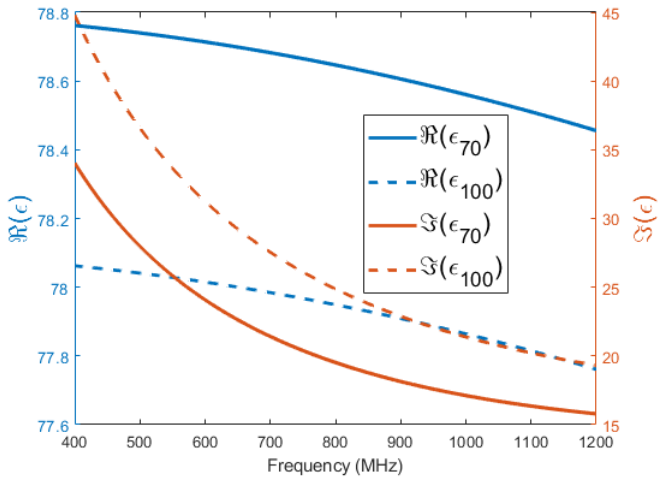

Figure 4.6: The real and imaginary parts of the permittivity of saline after increasing the salt concentration from 70 mmol (solid lines) to 100 mmol (dashed lines)

As can be seen, γ and α are almost frequency-independent, and β decreases considerably with frequency (around 10% in the considered frequency range). The reason is that the ratio between the coefficient behind γ which is $\frac{\sigma}{\omega\epsilon_0}$ and the coefficient behind α'', which is ϵ'', is decreasing across this frequency range. It means that the part that is increased, γ, is negligible in comparison to the constant (α''). Therefore, β is dominated by the change (α''). The two terms of the imaginary part of the permittivity and the ratio between these two terms are shown in Fig. 4.8 and its inset.

In paper E, it is further discussed how the changes in the parameter β is captured in the second-order derivative with respect to frequency. Under the assumption that the wave propagation can be described as a plane wave, an analysis of its amplitude is made in order to calculate the second-order derivative.

Based on these findings, a detection algorithm is proposed that categorizes the effects into four distinct types, defined by the sign of the relative signal change and its second-order derivative. Each of the fore cases are then as-

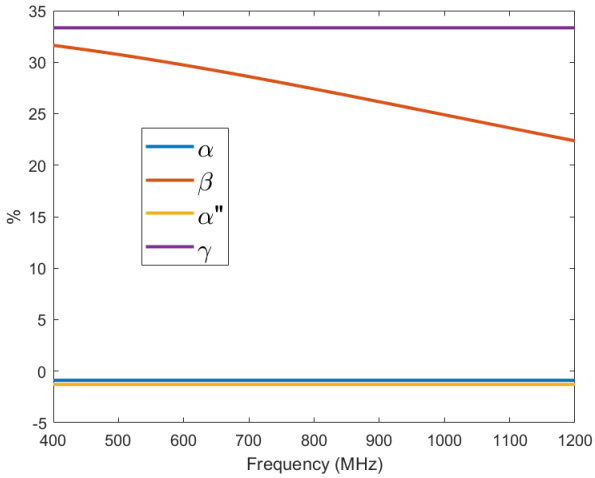

Figure 4.7: The Changes in the real and imaginary parts of the permittivity of saline after increasing the salt concentration

sumed to correspond to a specific physiological state or effect. The four types are summarized in 4.1.

Table 4.1: Relation between signal changes and permittivity changes

Type#	Signal change	Loss factor β	Physiological Effect
Type I	$\Delta_r < 0, \Delta_r'' > 0$	$\downarrow \beta > 0$	Inj. in the nonOcc. Ch.
Type II	$\Delta_r < 0, \Delta_r'' < 0$	$\uparrow \beta > 0$	Occ. in the nonOcc. Ch.
Type III	$\Delta_r > 0, \Delta_r'' < 0$	$\uparrow \beta < 0$	None
Type IV	$\Delta_r > 0, \Delta_r'' > 0$	$\downarrow \beta < 0$	Occ. in the Occ. Ch.

Type Detection algorithm

In this section the steps of a detection algorithm based on the theoretical findings introduced in previous chapters are discussed. Since the theoretical model is based on a plane-wave model, which is a very rough approximation of reality, further studies are needed before it can be concluded that the results are also applicable to 3D simulated or measured data.

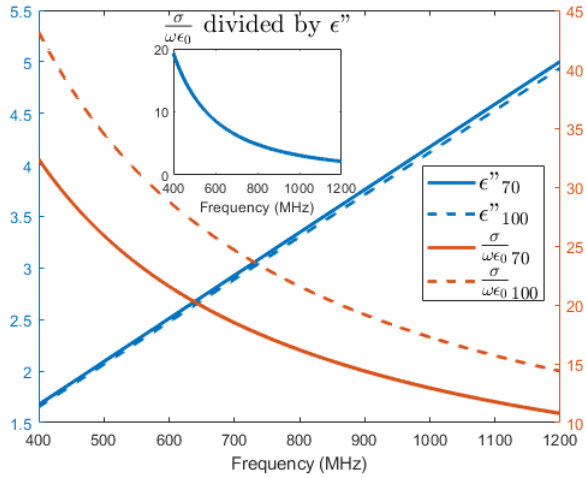

Figure 4.8: The two expressions in the imaginary parts of the permittivity of saline after increasing the salt concentration from 70 mmol (solid lines) to 100 mmol (dashed lines)

As a first step, we will filter out fluctuations caused by the resonances in the signal across frequencies. This is done through the isotonic filtration algorithm. Then, since the choice of the start frequency and end frequency of the signal affects the sign of the signal average and its second-order derivative, a window-based type detection method was developed. Finally, to enable the comparison of different channels and different animals while avoiding discretization of the type information into 4 discrete types, the phase that best captures the information of these signal types was defined.

Isotonic Filtration

As discussed above, unlike a plane wave, the simulated signal has a non-monotonic pattern, with large variations over the entire frequency band of interest. An example of such a signal is shown in Fig. 4.9 as the original signal. Even after the preprocessing introduced in [105], this signal varies sharply with frequency, as is shown by the black curve in Fig. 4.9. This makes it challenging to identify the overall trend of the signal and its second-

order derivative and correlate it with changes in the loss factor.

To tackle this issue, a novel signal filtering technique based on the Hodrick-Prescott filter [106] was proposed. This filter is useful to identify the overall trend in the data more effectively. The filter is applied iteratively to a signal until the second-order derivative becomes isotonic, i.e., it doesn't change sign over the frequency range. This filter inputs both the signal and a smoothing factor (λ). The output consists of the trend of the signal and its cyclical component. Increasing λ results in a smoother trend, while setting $\lambda = \infty$ yields the linear regression of the signal. The effect of the filtering is illustrated by one example in Fig. 4.9. This algorithm is detailed in Algorithm 2. The input is Δ_r, the relative differential signal. The isotonic function is called ISF that makes the second-order derivative of the input isotonic. The function hpfilter is the Hodrick-Prescott filter. The function SingChange checks if there's a change in the sign of its input and is defined in the last line of the algorithm.

Algorithm 2 Isotonic Filtration Algorithm

$\Delta_r = \text{ISF}(\Delta_r, \lambda)$
while SignChange(Δ_r'') **do**
    $\lambda = \lambda \times 1.1$
    $\Delta_r = \text{hpfilter}(\Delta_r, \lambda)$ ▷ Hodrick-Prescott filter
SignChange = $\exists\, i \in \{1, 2, \ldots, n-1\}$ such that $\Delta_r''(x_i) \times \Delta_r''(x_{i+1}) < 0$

The algorithm was further studied using 3D simulation data in paper E.

Window-Based Type Detection

In a realistic scenario of occlusion and injection, the change occurs in only one of several layers situated between the two antennas, making it necessary to perform an additional step to isolate and extract the relevant feature from the signal.

In this approach, the first frequency window is considered from $f_1 = 400$ MHz to $f_2 = f_1 + df$ MHz, where $df = 10MHz$. This value was selected because decreasing df further than 30 MHz did not change the signal type for any window. The next frequency window is considered by shifting the end frequency by another df which means $f_2 = f_1 + 2df$ and so on until f_2 reaches 1200 MHz. This is the 80th window. To construct the 81st window,

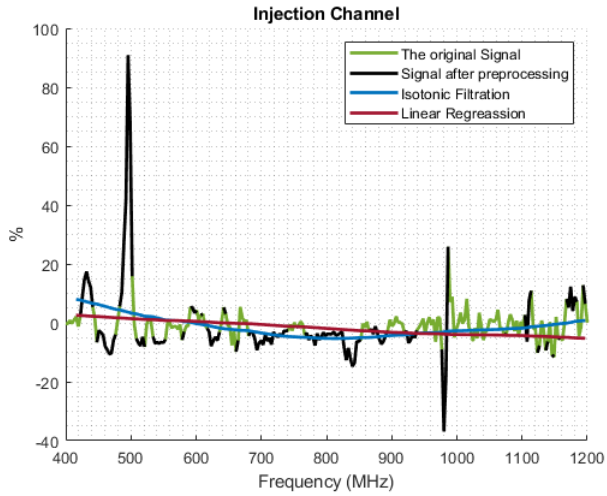

Figure 4.9: Comparison between the original relative differential signal (green), the signal after preprocessing (black), isotonic filtered signal (blue), and the linear regression of the signal (burgundy)

f_1 is shifted by df and the same process repeats. This procedure results in 325 frequency windows across the frequency range of 400–1200 MHz. This process is shown in Fig. 4.10.

After identifying the type of the signal, it is assumed that it is classified as type i within the frequency band t. In this case, the width of the window t is added to the ith column of a 1 by 4 zero vector. The overall signal type for that measurement instance is then determined based on the type with the maximum accumulated window width (AWW). The algorithm is outlined below in Algorithm 3 and in Fig. 4.11 as a flow diagram.

In this algorithm, the input is the differential signal Δ in the window ω_j, following a preprocessing step. Dividing it by the baseline signal, S_B, gave the relative differential signal. The isotonic filter is then applied, resulting in Δ_{pf}. Subsequently, the mean and second-order derivative of Δ_{pf} are calculated, producing Δ_r and Δ_r''. By examining the signs of these two parameters, a type is assigned to the corresponding window, and its width is accumulated in the associated element of N. This process is repeated until all windows have been evaluated.

Algorithm 3 Determination of Type

$\mathrm{N} = [0, 0, 0, 0]$
$f_1 = 400$ MHz, $f_2 = 1200$ MHz, $df = 30$ MHz
$t = 1$
for $i = f_1 : df : f_2 - df$ **do**
  for $j = f_1 + df : df : f_2$ **do**
    $S_{ij} = \mathrm{ISF}(S(i : j))$
    $\Delta_r = \mathrm{mean}(S_{ij})$
    $\Delta_r'' = \mathrm{mean}\left(\frac{d^2 S_{ij}}{d\omega^2}\right)$
    if $\Delta_r < 0$ **and** $\Delta_r'' > 0$ **then**
      $S_g(t) = 1$
    else if $\Delta_r < 0$ **and** $\Delta_r'' < 0$ **then**
      $S_g(t) = 2$
    else if $\Delta_r > 0$ **and** $\Delta_r'' < 0$ **then**
      $S_g(t) = 3$
    else if $\Delta_r > 0$ **and** $\Delta_r'' > 0$ **then**
      $S_g(t) = 4$
    $\mathrm{N}(S_g(t)) = \mathrm{N}(S_g(t)) + j - i$
    $S_f(t) = \Delta_r$
    $t = t + 1$
$Type = \max_i(\mathrm{N}_i)$ for $i = 1 - 4$
S_f=mean$(S_f(t))$ $\forall t \in \{S_g(t) = Type\}$

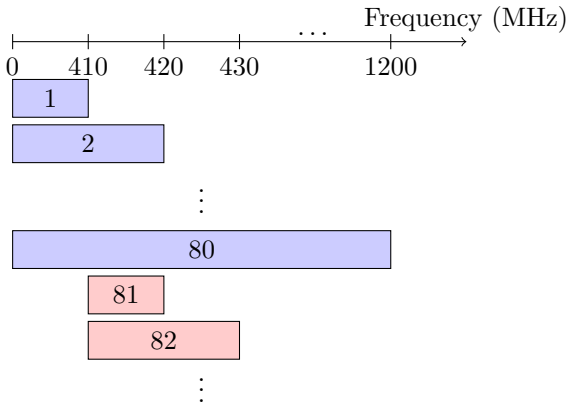

Figure 4.10: An illustration of the frequency windows. The number on each rectangle shows the frequency window number. The first and second iterations of constructing the windows are shown in lilac and pink colors, respectively.

To evaluate this method under more realistic conditions, another simulation study is conducted using a more realistic model of a sheep's head. In this case, changes are introduced to the permittivity and conductivity of the gray matter in one lobe of the brain, simulating the physiological effects of the occlusion or the injection, as illustrated in Fig. 4.12. The simulation setup is the same as in [105]. Two separate simulations were made. In simulation 1, both the real and imaginary parts of the relative permittivity of the gray matter are increased by 10% on the non-occluded side which resembles the dielectric change due to the occlusion. In simulation 2, only the imaginary part of the relative permittivity of the gray matter is increased using the same coefficients as β_1 in Fig. 4.7.

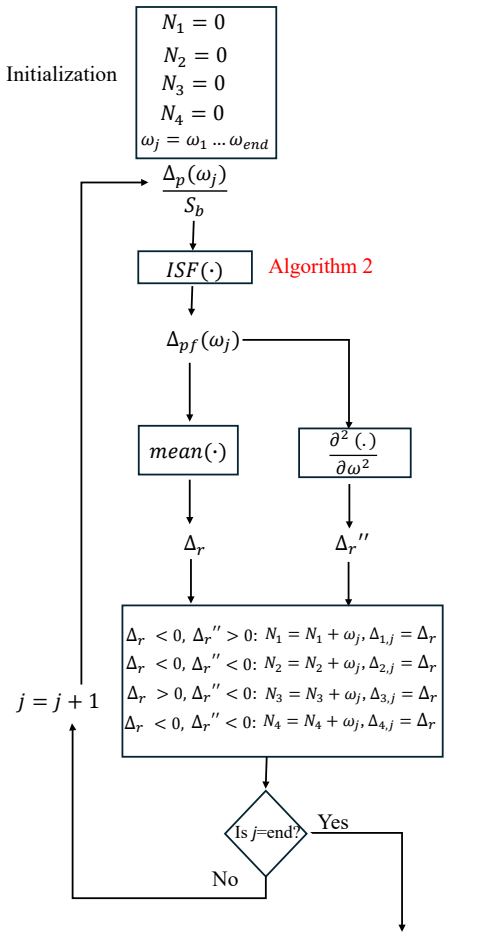

1. The signal Type is the one that has the largest N.
2. $S_f = mean_j(\Delta_{\text{Type},j})$
3. $\phi = \tan^{-1}\left(\frac{N_i - N_j}{N_i - N_k}\right) + \frac{4-i}{2}\pi$
4. $N_x = \frac{N_i}{N_c}$

Figure 4.11: Flow chart of the type detection algorithm. The input to this algorithm, Δ_p, is the output of the preprocessing algorithm, and ISF is the isotonic filtration.

Table 4.2: complex dielectric values of the considered tissues in the Simulation at 800 MHz

Tissue	Complex Permittivity
Bone	$12.5 - 2.92j$
Muscle	$55.3 - 20.2j$
Fat	$11.4 - 2.2j$
Grey matter	$53.25 - 20.2j$
White Matter	$39.2 - 12.6j$
Cerebrospinal Fluid	$68.9 - 53.27j$

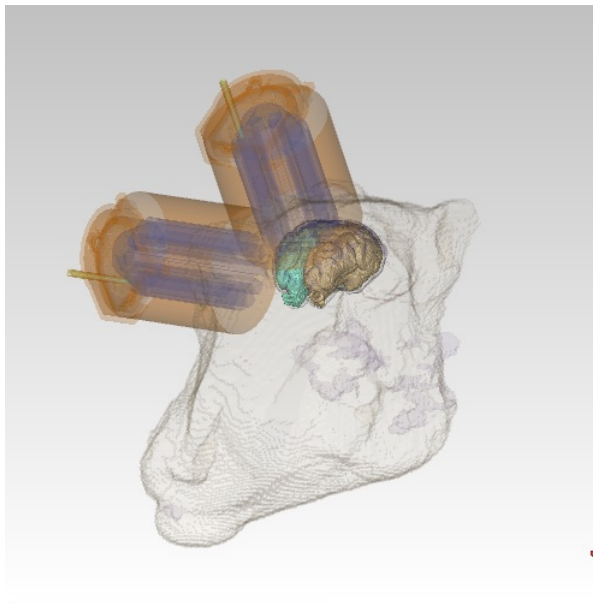

Figure 4.12: The setup of the simulation of the antennas on a sheep's head to model the occlusion and injection. The turquoise color shows the area of the brain where the complex permittivity has changed.

In this simulation scenario, which deviates significantly from a plane wave model, the transmission between the two antennas is highly prone to multi-path interference, making it challenging to extract a stable trend across the

entire frequency band. To address this, it is proposed to divide the frequency band into multiple windows. By identifying the type of signal for each frequency window, the probability of each type can be calculated over the entire band. The window-based type detection algorithm is described in detail in the Appendix. The output of this algorithm is the accumulated window width (AWW) for each type. A vector of four elements, initialized to zero (one element per signal type), is used to track the AWW. Whenever a window is classified as a certain type, the width of that window is added to the corresponding element in the AWW vector. After all windows have been processed, the type associated with the highest AWW value is designated as the overall signal type.

Using this algorithm, the occlusion and injection events were successfully identified by analyzing the transmission data obtained from the simulations. The results of the window-based type detection algorithm are presented in Fig. 4.13. This figure illustrates the AWW on the y-axis for each type on the x-axis for the two simulations. As shown, the AWW for Type II is the highest in Simulation 1, whereas in Simulation 2, as expected, Type I exhibits the maximum AWW. The selected type in each case is highlighted with the corresponding color scheme outlined in Table 4.1, while non-selected types are displayed in black for clarity.

From discrete type to continuous phase

To investigate if this type-classification behaves the same on the data measured on all animals, we need to extend the definition of the types. Since classifying the signals into four discrete categories represents a form of discretization, it limits the ability to subtract the signal type in one channel from that in another or to compute the mean type across different animals.

To transform this discrete classification into a continuous, comparable, and quantifiable measure, a new variable is needed. Such a variable puts the four elements of the AWW vector into a single unique continuous variable. It is defined as follows:

$$\phi = \tan^{-1}\left(\frac{Ni - Nj}{Ni - Nk}\right) + \frac{4 - i}{2}\pi \tag{4.12}$$

where N_i shows AWW of type i, N_j shows the AWW for the type that the sign of Δ_r differs from the sign of Δ_r in i and N_k shows AWW for type that the sign of Δ_r'' differs from the sign of Δ_r'' in i. For example, if a signal classified as type

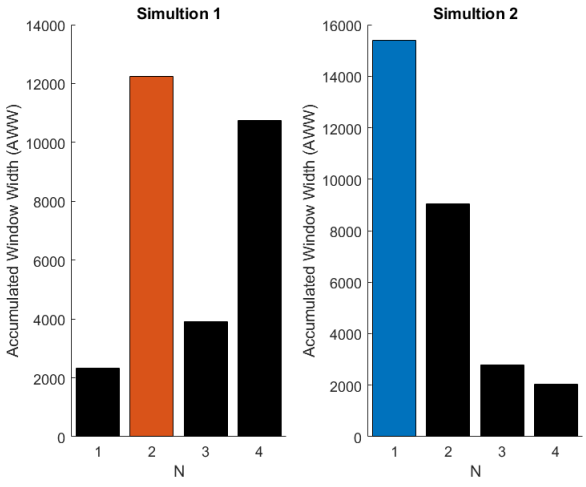

Figure 4.13: The results of applying the window-based type detection method on the simulated data of the antennas on the sheep's head. Simulations 1 and 2 are the occlusion and injection scenarios, respectively. The y-axis shows the AWW, and the x-axis is each type.

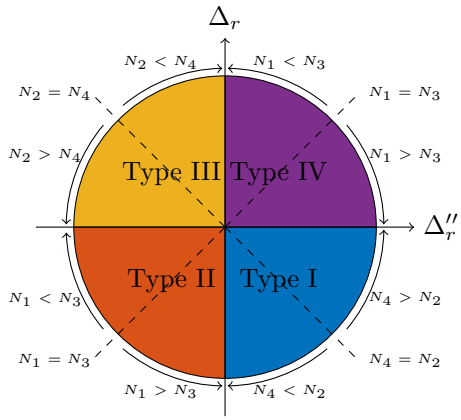

Figure 4.14: Each type is assigned to a quadrant, where the radius in the middle of each quadrant shows when the type has the highest probablity

I exhibits strong characteristics, the variable ϕ tends toward $\frac{7\pi}{4}$. Conversely, if the ϕ value of this signal approaches 2π, it may be misclassified as type IV. Additionally, if ϕ tends toward $\frac{3\pi}{2}$ the signal could be confused with type II. Applying this notion, it can be shown that by transferring the signal to a polar coordinate, each type could be assigned to a quadrant. The relationships between the quadrants and the corresponding signal types are illustrated in Fig. 4.14.

The developed algorithm's complete flow chart is shown in Fig. 4.15. This flow chart is divided into preprocessing and processing parts. The subscript i stands for the non-occluded channel mostly affected by the injection, o for the occluded channel, and b for the baseline data.

The final output is acquired by subtracting the window-based type detected signal of the occluded channel from its non-occluded channel counterpart (indicated with the circle at the bottom of the figure) to form a differential complex signal ΔS_C. This output represents a measure of asymmetry between the two channels.

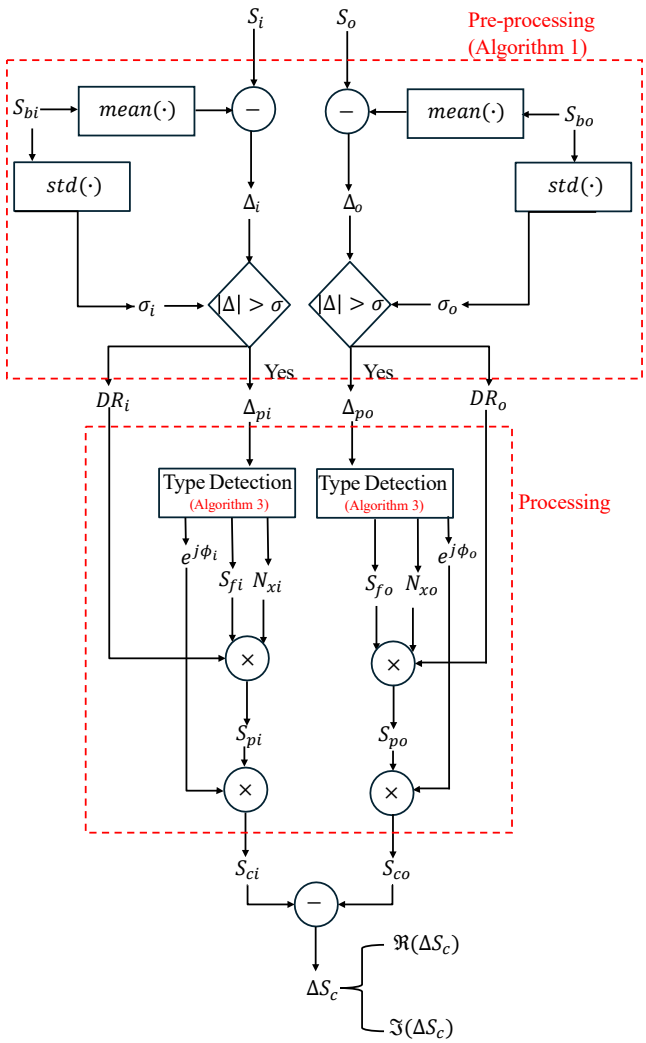

Figure 4.15: The complete flow chart of the signal processing algorithms

4.3 Results

In this section, the results of the proposed microwave detection algorithm on the experimental data are presented. First, the results for one animal are presented and compared with the results for the other animals.

An Example of Microwave Detection Results

Before presenting the results of the microwave detection, all the processing steps are summarized. First, the measured relative differential signals Δ_r are calculated in the preprocessing step. From here the algorithm outputs a signal containing only elements whose power exceeds the noise threshold, along with a detection rate (DR). Next, these signals are passed to the type detection algorithm, which provides two sets of information for each measurement: the signal amplitude and the signal type.

To classify the signal based on its assigned type, all signal amplitudes are averaged across all windows classified as that type, referring to this averaged value as S_f. A complete definition of S_f can be found in Algorithm 3 in section 4.2. The type information itself is encoded in the phase, except for one additional piece of information: the accumulated window width (AWW) for the type that has both Δ_r and Δ_r'' with opposing signs, denoted as N_c. This is incorporated into a parameter defined as $N_x = \frac{N_i}{N_i+N_c}$ where N_i is the AWW of the selected type. To encompass the information provided by all these parameters, a new parameter is defined in Eq. 4.13.

$$S_p = S_f \times N_x \times DR. \tag{4.13}$$

The results of microwave detection for the three stages of the measurement on animal 1 are shown in Fig. 4.16 for the injection and occluded channels, respectively. In this figure, the color of the bars shows the signal type. The height of each bar is S_p. A larger S_p means a stronger change was measured compared to the baseline signal. It is seen in the occlusion+injection stage, as expected, the first few measurements of the non-occluded side are of type II which shows the effect of the occlusion. After that, the third measurement is a type I change, which shows the effect of the injection. In contrast, on the occluded channel, after the first negative measurement, there is a train of positive signals of types III and IV, which are the expected changes on the occluded side according to table 4.1.

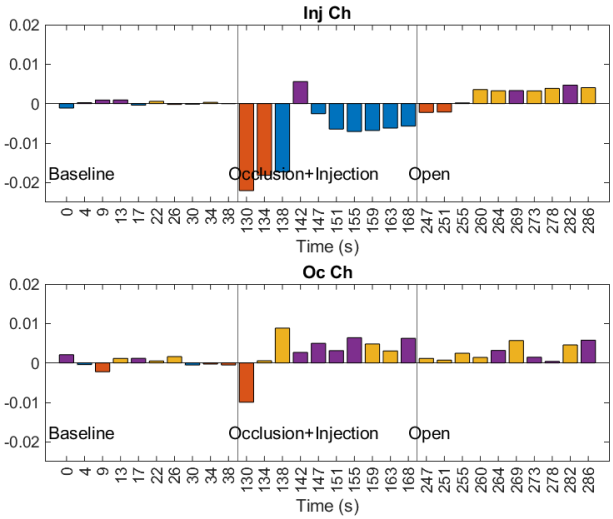

Figure 4.16: S_p in both channels, Animal 1

Comparing Measurements of animals

To compare the result of the animals and find the asymmetry between the two channels, both the bar height S_p and the phase ϕ are incorporated to create a complex vector for each of the two channels:

$$\Delta S_c = S_{co} - S_{ci} = S_{po}e^{j\phi_o} - S_{pi}e^{j\phi_i} \tag{4.14}$$

The imaginary part of this complex vector reveals the sign and amplitude differences between the two signals while subtracting the real part of one signal from the other indicates the distance in terms of the second-order derivative.

As the amplitude of the non-occluded channel approaches negative values, the opposite occurs for the occluded channel; thus, the imaginary part of ΔS_c should exhibit a positive sign, as illustrated in Fig. 4.17. Conversely, a positive second-order derivative signifies the influence of the injection, indicating that the real part of ΔS_c should trend toward negative values, as shown in Fig. 4.18.

To generate these figures, the signals for animals 3 and 4 were normalized

to the occlusion stage of their measurements, ensuring alignment with the timing of animals 1 and 2 and enabling calculation of the average across all four animals.

In these figures, the asterisk (*) denotes a statistically significant change in the maximum absolute value of the data across each stage, while "ns" indicates that the p-value of the permutation test was below the threshold of 5%.

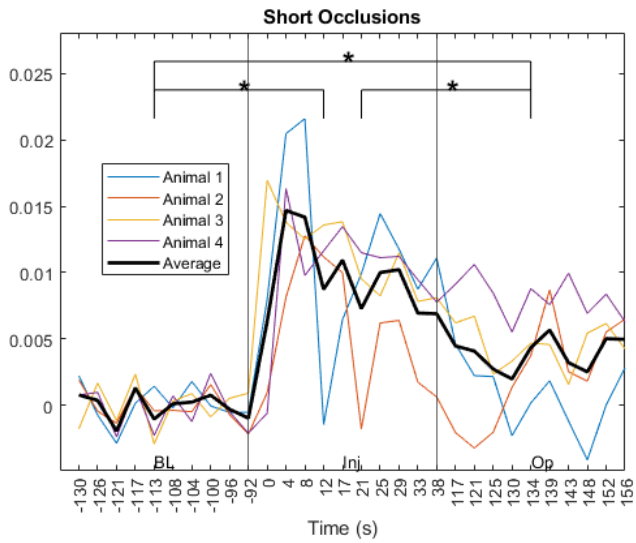

Figure 4.17: The imaginary part of ΔS_c for the short occlusions

The imaginary part of ΔS_C for the long occlusions is shown in Fig. 4.19. As is seen in this figure, unlike the short occlusions, the simultaneous increase in the non-occluded channel and decrease in the occluded channel results in a negative value for ΔS_C.

4.4 Chapter Summary and Conclusion

In this chapter, two signal processing algorithms were introduced to analyze the measured microwave signals. The first focuses on detecting deviations from the baseline based on signal power, while the second algorithm establishes a link between the observed changes and the underlying physics of conductivity

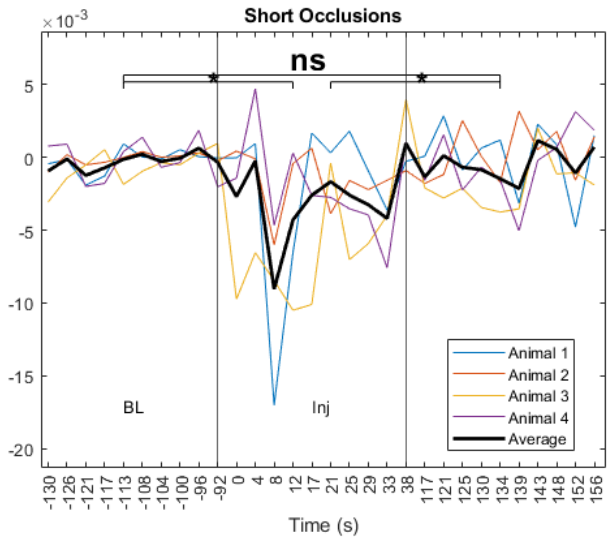

Figure 4.18: The real part of ΔS_c for the short occlusions

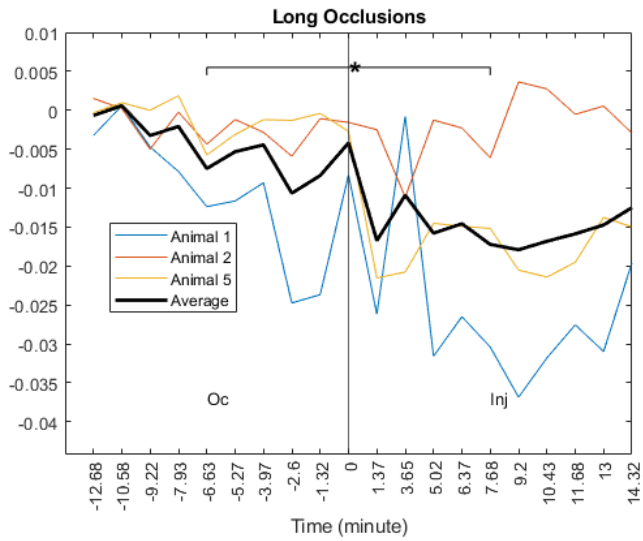

Figure 4.19: The imaginary part of ΔS_c for the long occlusions

enhancement. A thorough discussion of the results and their interpretation is provided in the following chapter.

CHAPTER 5

Pathophysiology of Ischemic Stroke

In the previous chapter, the microwave detection results for large vessel occlusion were introduced. Since interpreting these findings requires a deeper understanding of the pathophysiological processes triggered by arterial occlusion and saline injection, this chapter begins by examining the pathophysiology of ischemic stroke. Subsequently, CT scan data are presented and analyzed to study the hypothesis concerning the effects of prolonged occlusion on the brain.

5.1 Pathophysiology of Occlusion and Injection

Assessing the pathophysiological effects of arterial occlusion and injection is not straightforward. Multiple effects of variable strengths can affect the animal simultaneously. As an example, the occlusion may decrease the measured microwave amplitude of a wave propagating through the non-occluded side of the brain due to an increased blood flow on that side. Baldwin et. al. [107] found that the increased blood flow on the collateral side in a similar sheep model was not a result of a rise in mean arterial pressure (MAP); but rather a result of vasodilation allowing more blood volume on the non-occluded side.

However, this effect can in turn also reduce the CSF volume on the non-occluded side due to cranial compartment inter-dependencies. Furthermore, with a decreased blood flow and volume on the occluded side, Mestre et. al. have shown that the resulting imbalance of partial water pressure can result in an influx of CSF into the brain tissue of the occluded part of the brain. On the longer time scales, they also showed that the resulting ionic imbalance can have a similar effect [108]. As a result, CSF can accumulate on the occluded side of the brain and diminish on the non-occluded side. This accumulation and reduction are called "CSF influx" and "CSF shortage" respectively. This CSF influx is not limited to focal ischemic stroke but is also found in anoxic stroke, where the whole brain is deoxygenated [109].

It should be mentioned that the injection also affects the CSF influx into the brain. In recent studies, it was found that the intravascular injection of hypertonic saline increases the CSF influx and reduces the brain size [110]–[112].

These processes are depicted in Fig. 5.1. In this figure, the top panel shows the physiology of a normal brain where the blood vessels are separated from the brain tissue by a semipermeable membrane called the blood-brain barrier (BBB) formed by the astrocyte endfeet [113]. The lymphatic pathway is shown by the narrow, light blue area filled with CSF. After the occlusion, the blood volume is reduced on the occluded vascular territory. Since according to the Monro-Kellie doctrine [114], [115] the total volume of fluids in the cranial compartment is fixed, a reduction in the blood volume results in an increase in the CSF volume. In a rodent model, this influx of CSF can occur as fast as 11 seconds after the arterial occlusion [108]. A second wave of CSF influx happened 5 minutes after the occlusion due to the spreading depolarization in that animal model. The bottom panel shows the potential pathophysiological processes caused by the injection which are a drainage of water from the brain and at the same time, more CSF influx [110]–[112]. It should be noted that edema at this hyperacute phase of the ischemic stroke happens with an intact BBB [116].

Timeline of the Pathophysiological Effects

To summarize and facilitate the interpretation of the results, a timeline can be established to outline the sequence of physiological events occurring during both short and long occlusions such as occlusion, injection, and CSF dynamics.

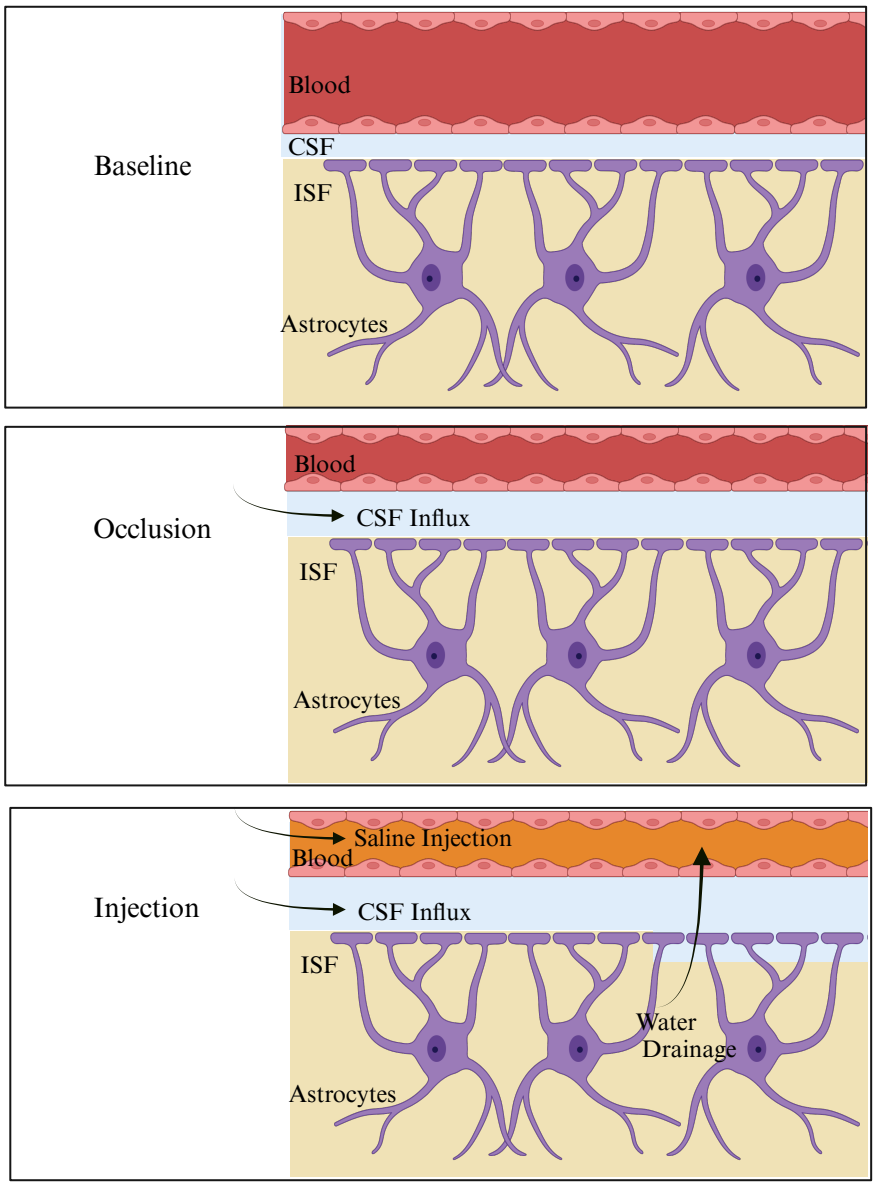

Figure 5.1: Normal physiology of the brain during the baseline (top), followed by the pathophysiological processes of the occlusion (middle) and the injection (bottom). CSF: cerebrospinal fluid; ISF: interstitial fluid. The image was created with BioRender.com.

These timelines provide a structured approach to understanding the progression of these effects and enable a clearer analysis of the temporal relationships between different physiological changes. In figures 5.2, 5.3, and 5.4, these timelines are illustrated for the short and long occlusion cases, respectively.

Throughout this section, a change means a change in the amplitude of the measured received microwave signals either after the blockage of the arteries in the left hemisphere or after the venous injection of saline solution. This change can be either an increase, indicating a decrease in the attenuation of the microwave signal in that region, or it can be a decrease in signal level, indicating an increase in the attenuation.

Starting with the short occlusions, Fig. 5.2 indicates the simultaneous effect of the occlusion and injection on the non-occluded side as discussed above. The negative signs here represent the decreased microwave transmission through the non-occluded side of the brain resulting from both blockage due to the increased blood volume on the non-occluded side and injection of the saline solution. In the same way, the positive signs in the figure indicate the increased transmission of microwave signals in the occluded side as a result of the decreased blood volume. The "No effect" of the injection indicated in the figure is an assumption based on the finding by Baldwin et. al. [117] who saw no initial collateral flow following an occlusion.

Continuing with the long occlusions, starting with the non-occluded side, Fig. 5.3 indicates the simultaneous effect of the blockage, injection, CSF shortage, and CSF influx as discussed above. Because of the long occlusion, the effects are now time-dependent as indicated in the picture. In the initial phase, the effect of the occlusion and the CSF shortage is present, and following that, the negative signs represent the decreased transmission of microwave signals through the non-occluded side of the brain resulting from the occlusion, and the positive signs indicate the increased transmission of microwave signals as a result of the CSF shortage. After the injection, there is a negative effect caused by the injection on the non-occluded side. This injection can drain the interstitial fluid due to the osmolarity imbalance but might, on the other hand, also increase the CSF influx to the area it reaches, according to the finding in [112]. These two effects act in different direction are shown by the negative and positive signs in Fig. 5.3.

Finally, the effect of the long occlusions on the occluded side of the brain is considered. Here the dynamics are different from those of the non-occluded

side. As is shown in Fig. 5.4 the effect of the occlusion on the occluded side of the brain, is first that the measured microwave will increase in magnitude. This is because the blood flow and blood volume are decreased. This increase is shown with the positive signs in this figure. Then, following the occlusion, an influx of the CSF into the brain tissue can be anticipated to compensate for the loss of pressure caused by the diminishing blood volume. Then, in turn, after the injection, collateral blood flow can be expected. Then one can expect to see an increasing blood volume on the occluded side of the brain. This would result in a decrease in the measured microwave signals which is shown by the negative signs after the injection in Fig. 5.4. The saline injection can then, in turn, due to the collateral flow, cause either more influx of the CSF to the brain parenchyma or drainage of the water from interstitial space due to osmosis on the occluded side of the brain.

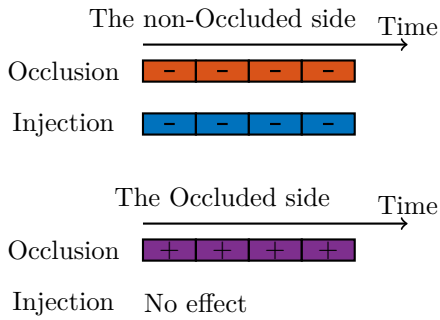

Figure 5.2: Comparison of the two channels during the Short Occlusions. The positive and negative signs represent the increased and decreased transmission of microwave signals, respectively.

5.2 CT scan analysis

To study the hypotheses about the physiological underpinnings of the changes observed during the long occlusions, a series of CT scans was performed before and after the long occlusions. The animal was positioned within a CT gantry, with scans performed at a resolution of 0.5 × 0.5 × 0.5 mm. Angiographic CT was performed using an iodinated contrast agent that was introduced, enabling visualization of vascular structures in detail.

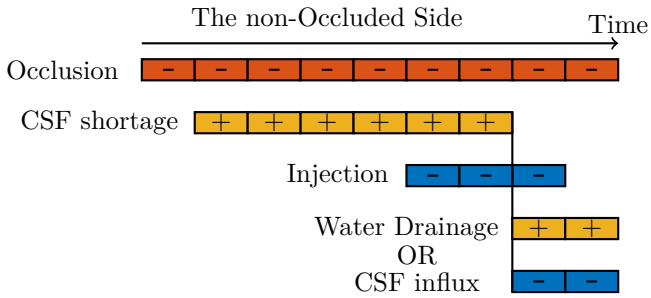

Figure 5.3: Simultaneous physiological effects on the non-occluded side during the Long Occlusion. The positive and negative signs represent the increased and decreased transmission of microwave signals, respectively.

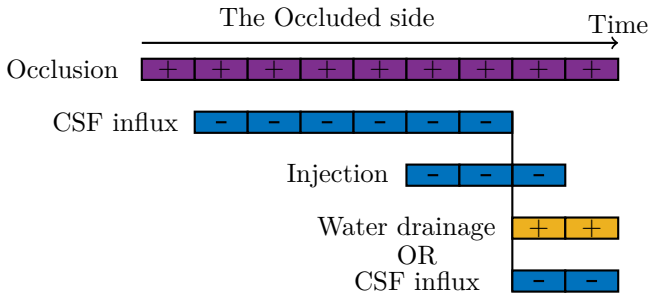

Figure 5.4: Simultaneous physiological effects on the Occluded side during the Long Occlusion. The positive and negative signs represent the increased and decreased transmission of microwave signals, respectively.

Early signs of stroke in the brain, can be detected through changes in Hounsfield Unit (HU) values of gray matter regions, specifically the caudate nucleus (CN), situated beneath the ventricles within the basal ganglia. This area is known to exhibit early effects during stroke events [118]. It is shown that sheep's brain also poses a similar area [119]. The hypothesis is that water may shift from the ventricles into surrounding regions, including the CN, resulting in a decrease in ventricular volume and a lower HU in the CN on the occluded side compared to the open side.

For this analysis, the ventricles were segmented, and circular areas were identified above and below them to locate the CN on both the occluded (left)

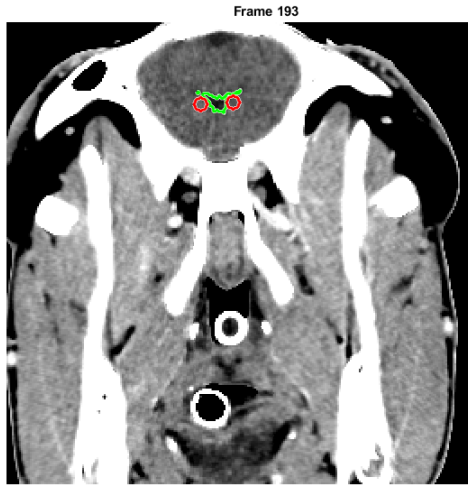

Figure 5.5: A slice of the CT scan with lateral ventricle segmented (Area with Green boundary) and the Caudate Nucleus segmented (Red Circles)

and open (right) sides. Ventricle segmentation was performed by setting a threshold around the HU value characteristic of cerebrospinal fluid (CSF). A total of 21 slices were used for segmentation of the ventricle. Once segmented, the ventricle was divided into left and right halves. The center point of each half was used to define a circular region with a radius of 3 mm, positioned tangentially to the ventricle on the x-axis. An example slice from these CT scans is shown in Fig. 5.5.

CT Scan analysis results

In this subsection, the results from the CT scan analysis are presented. As described in the previous section, an influx of CSF is indicated by a reduction in ventricle size and a decrease in HU values in the surrounding gray matter tissue [118], [120].

The CT scan analysis is based on a criterion, C which is satisfied when two conditions are met: a decrease in HU value on the occluded side, and a shrinkage in ventricle size in the same location. The aim with the analysis was

to assess how much of the caudate nucleus (CN) volume satisfies C following a long occlusion. If a larger proportion of the CN satisfies C after the occlusion, this supports the hypothesis that CSF from the ventricles has moved into the surrounding brain tissue. To get a better understanding of the defined criterion, it is depicted in Fig. 5.6. In this figure, C is shown as a shrunk ventricle with darker CN indicating a lower HU while $\sim C$ is all the other three possible cases. It should be noted that the cases where the ventricle size is identical on both sides or the HU is exactly the same on both sides are rare and thus not depicted.

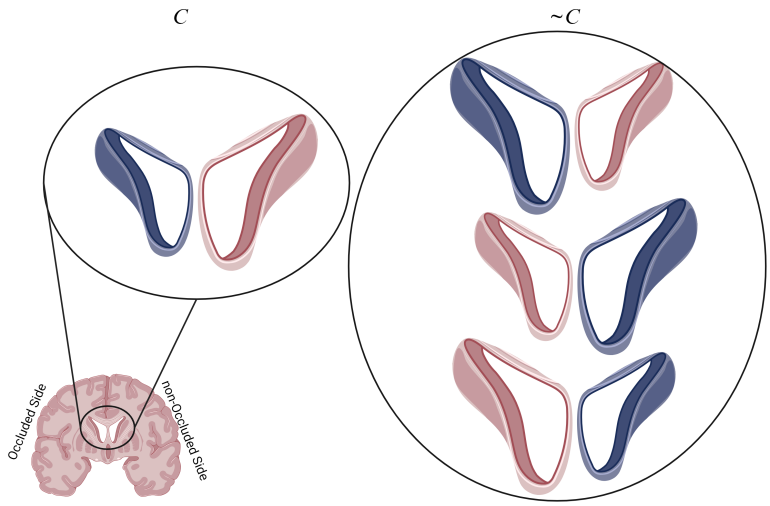

Figure 5.6: C is shown as a shrunk ventricle with darker CN indicating a lower HU while $\sim C$ is all the other three possible cases. The image was created using BioRender.com.

This result is illustrated in Fig. 5.7. The left two bars in the figure represent the percentage of CN volume where C is satisfied, with the blue bar indicating the volume before occlusion and the red bar after. The two bars on the right show the percentage of CN volume where is not satisfied. The data suggests that a larger proportion of the CN displays signs of potential edema after the occlusion, likely caused by an influx of CSF from the ventricles after the occlusion.

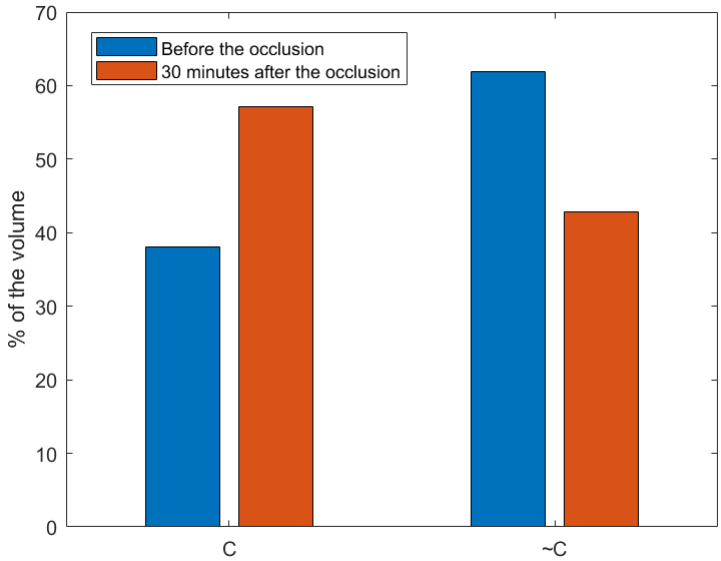

Figure 5.7: The percentage of the volume of Caudate Nucleus where C is satisfied before (blue) and after (red) the occlusion. The C criterion is satisfied when a decrease in HU value occurs on the affected side, and at the same locations, a shrinkage in ventricle size is observed. $\sim C$ is when either of the conditions are not met.

5.3 Chapter Summary and Conclusion

In this chapter, the potential pathophysiological effects triggered during the experiments were discussed. It helped with the interpretation of the results presented in the previous section.

In Fig. 5.8, as the final summary, the condition of a schematic brain during the three stages of the long occlusion experiment is shown. The experiment starts with a symmetric brain during the baseline. The occlusion could result in CSF influx to that brain tissue; therefore, the ventricle on the left becomes smaller. After the injection, interstitial fluid from the right side can be removed; therefore, the brain is shown as dehydrated tissue.

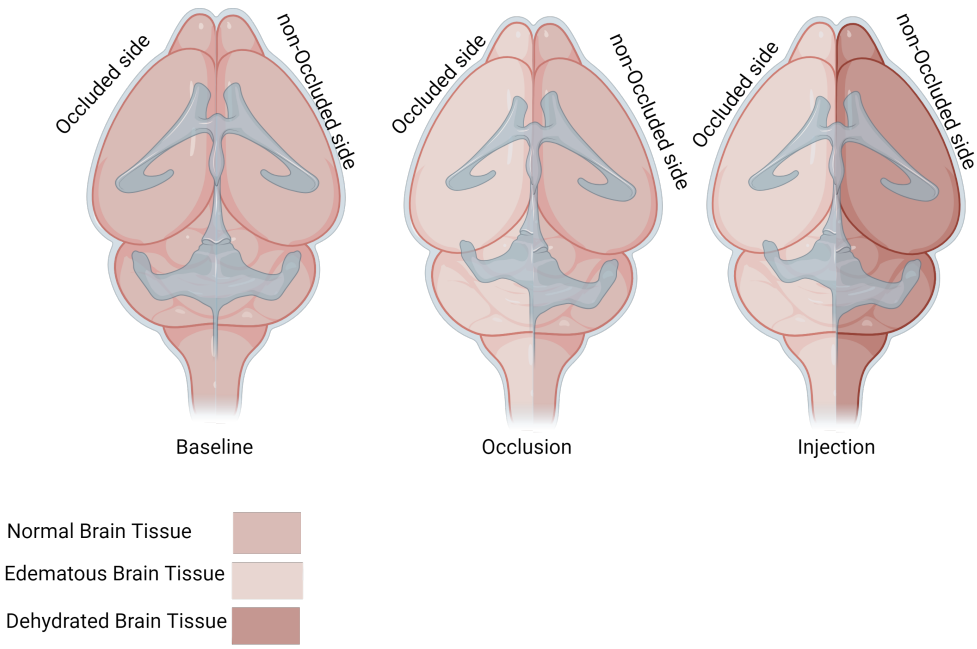

Figure 5.8: Changes in the brain during the three stages of the experiment. The image was created using BioRender.com.

The results highlight compelling aspects of stroke pathophysiology and demonstrate how these may be detected via microwaves. However, further experimentation is essential before any firm conclusions can be drawn regarding the hypothesized CSF influx or shortage. Moreover, to fully establish the accuracy of the detection method, additional data from larger sample sizes and controlled experiments are necessary to validate and confirm these findings.

CHAPTER 6

Summary of included papers

This chapter provides a summary of the included papers and the contributions of the author of the thesis to each papers.

6.1 Paper A

Seyed Moein Pishnamaz, Xuezhi Zeng, Hana Dobšíček Trefná, Mikael Persson, Andreas Fhager
Reducing Waves on the Body Surface in Near-Field Medical Diagnostics by a Dielectric Rod Antenna
IEEE TRANSACTIONS ON ANTENNAS AND PROPAGATION, VOL. 71, NO. 10, OCTOBER 2023.

The multipath interference caused by the waves traveling on the body surface is a factor that limits the detection accuracy of microwave-based biomedical diagnostic systems. The waves traveling along these paths do not carry information about the area of interest inside the body, but are more sensitive to changes in dielectric properties close to the antennas. In this article a new antenna has been designed vy placing a dielectric rod between the radiating

element of the antenna and the body. This results in a significant reduction of surface waves while the antenna remains matched to the body. The dielectric rod antenna (DRA) was designed by deriving a 2-D analytical solution of the wave propagation in a two-layer cylindrical structure. The design is extended to 3-D and further optimized using numerical simulations. It was shown that the addition of the dielectric rod enhances the field confinement by a factor of 2. The performance of the antenna, as verified by phantom measurements, shows that the DRA increases the ratio of the transmission coefficient to power on the body surface to up to 24 dB and the antenna bandwidth is increased by 71% compared with the antenna without the dielectric rod.

Contribution

The author of this thesis suggested that a dielectric rod antenna could solve the problem of reducing multi-path signals. The author of this thesis further performed all the calculations, designed and built the antenna, performed experiments, and analyzed the results. Finally, The author of this thesis took on the main responsibility of writing the manuscript with the help of the co-authors.

6.2 Paper B

Seyed Moein Pishanamz, Andreas Fhager, Mikael Persson
Analysis of the 2D Guided Mode Propagation in a 3D Dielectric Rod Antenna
17th European Conference on Antenna and Propagation, 2023.

This paper presented a 2-dimensional guided mode propagation analysis and compared the results to a 3-dimensional dielectric rod antenna. An approximated model based on the summation of the guided modes multiplied by the coefficients obtained by projecting the 3D fields on the 2D fields is derived and the accuracy is investigated. The factors playing a role in the error of the approximation are studied and it is concluded that the main cause of error in the guided mode propagation approximation is the reflection from the truncation at the end of the rod rather than the radiating field along the rod.

Contribution

The author of this thesis has performed all modeling, simulations, and calculations, performed the analysis, and written the manuscript.

6.3 Paper C

Seyed Moein Pishnamaz, Xuezhi Zeng, Hana Dobšíček Trefná, Mikael Persson, Andreas Fhager
Asymmetry Detection in a Noisy Microwave-Based Biomedical Diagnosis
2024 IEEE MTT-S International Microwave Biomedical Conference (IMBioC).

This paper demonstrates the initial investigations with the Signal Power Comparison Algorithm for the Detection of Anomalies (SPCADA). Here the method was tested on data obtained from a numerical 2-dimensional simulation of an asymmetrical structure. The asymmetry is created by varying the real and imaginary part of the permittivity in one-third of the diagnosis domain where 3 antennas that form 2 symmetric channels are used. It is shown that even with a simple diagnosis algorithm, the accuracy can be improved by using the information from both channels.
Contribution
The author of this thesis has performed all modeling, simulations, and calculations, performed the analysis, and written the manuscript.

6.4 Paper D

Seyed Moein Pishnamaz, Xuezhi Zeng, Hana Dobšíček Trefná, Mikael Persson, Andreas Fhager
Microwave-Based Detection of Large Vessel Occlusion Using Contrast Enhancement
To be submitted to IEEE Transactions on Biomedical Engineering.

This paper introduces a novel approach for detecting large-vessel occlusion using microwave measurement measurements. The approach utilizes a setup with three antennas configured in a two-channel microwave transmission system, designed to detect asymmetric dielectric changes in the brain induced by occlusion of a blood vessel and by a contrast-enhancing intravenous saline injection. An algorithm has been developed to analyze the microwave data obtained before and after injection, evaluating changes in the signal's power across frequencies. The method was tested on a sheep model, leveraging its

similar head size and structure to that of humans. The results indicate that the proposed method can detect changes associated with the occlusion and injection phases, effectively distinguishing these from baseline and post-occlusion states. This approach highlights the potential of microwave-based diagnostics in detecting critical brain events with high sensitivity.

Contribution

The author of this thesis has participated in the planning and in performing of the experiments together with the co-authors and the collaborators at the Norwegian University of Life Science. The author of this thesis has proposed the analysis method and performed the simulation, written the code, and analyzed the measurement data. The author of this thesis has written the manuscript with the help of the co-authors.

6.5 Paper E

Seyed Moein Pishnamaz, Xuezhi Zeng, Hana Dobšíček Trefná, Mikael Persson, Andreas Fhager

Microwave-Based Detection of Large Vessel Occlusion Using Contrast Enhancement- A Frequency-Derivative Analysis

To be submitted to IEEE Transactions on Biomedical Engineering.

In this paper, the analysis of the experimental measurement data from the sheep experiments presented in paper D has been extended. A method was developed aiming at evaluating changes in the transmission signal's sign and its second-order derivative across frequencies and relating that to dispersive characteristics of changes in the brain's conductivity during the injection and occlusion experiments. This algorithm was developed based on theoretical analysis and simulations. The study demonstrated that the developed algorithm could classify injection and occlusion effects in both simulated and real animal models. Overall, this work not only advances the understanding of the differentiation between occlusion and injection but also establishes a framework for detailed analysis.

Contribution

The author of this thesis independently came up with the idea of relating the changes in the measured microwave signals to dielectric changes and further connect them to the physiological effects of occlusion and injection. The author of this thesis developed the idea and algorithms, has written the codes,

performed the simulations, and done the analysis of the measurement data as well as written the manuscript with the help of the co-authors.

6.6 Paper F

Seyed Moein Pishnamaz, Xuezhi Zeng, Hana Dobšíček Trefná, Mikael Elam, Andreas Fhager, Mikael Persson
Investigating the Effects of Saline Injection as a Contrast Enhancement Agent in Microwave Diagnostics of Large Vessel Occlusion
To be submitted to Stroke Translational Research.

In this paper, an in-depth analysis and discussion are presented to investigate how the changes observed in the microwave data correlate with both the injection and occlusion experiments in sheep, as well as with known physiological processes in the brain. Short and long occlusions were specifically designed to reveal detectable asymmetries in blood flow and edema formation within the animal model. CT scans were performed and analyzed to validate the hypothesis regarding the physiological origins of the observed changes.
Contribution
The author of the thesis has participated in the planning, designing, and performing of the experiments together with the co-authors and collaborators at the Norwegian University of Life Science. The author of this thesis has proposed the analysis method of the measured microwave signals and CT scan images and performed the analysis. The author of the thesis has written the manuscript with the help of the co-authors.

CHAPTER 7

Conclusion and Future Work

In this thesis, the background and findings are presented of the efforts to develop a technique for detection of large vessel occlusion in the brain using microwave technology. The primary goal has been to develop a detection device capable of identifying thrombectomy candidates so that these patients can be transported more quickly to thrombectomy centers than today.

The research focused on three main areas:

- Designing an antenna suitable for the measurement setup,
- Developing measurement protocols for the animal study, and
- Creating signal processing algorithms to analyze and interpret the measured microwave signals.

7.1 Antenna Design

The design and the development of an antenna that minimizes surface waves around the body are presented. The antenna was engineered to deliver sufficient power to the body while maintaining a high gain and low return loss.

This was achieved by placing a dielectric rod in front of the radiating element and converting a self-grounded bow-tie antenna (SGBTA) into a dielectric rod antenna (DRA). We demonstrated that this design reduces surface wave power by up to 10 dB compared to the SGBTA. Moreover, the DRA exhibited a significantly more stable gain across its operational frequency range, as well as a 72% increase in bandwidth compared to the previous design. Using three such antennas, an experimental prototype system was built, and the possibility of detecting asymmetries in the brain caused by large vessel occlusions and subsequent saline injections was studied.

7.2 Animal Model Development

Another main goal of this highly exploratory research, conducted over several years and involving multiple animals, was to optimize measurement setups, protocols, and signal processing algorithms. A key part of this effort was the development of a new procedure and protocol for animal studies of these aspects, which to the best of our knowledge had not been done before. Ultimately, it was concluded that to maximize the detectable asymmetry without interference from collateral flow, both the common carotid arteries and vertebral arteries had to be occluded, followed promptly by the injection of a contrast enhancement agent. The injection dosage was chosen to remain within a safe range suitable for eventual human application while still generating detectable changes in the measured signals. In paper D, a detailed calculation for the injection dosage is provided.

7.3 Signal Processing

The effect due to the changes in the brain's asymmetry is very small, making it impossible to detect the changes by just inspecting the raw microwave data. Instead, two different signal processing algorithms were developed for the analysis. The first algorithm detects deviations from a baseline reference measurement by detecting changes in the signal power. The second algorithm links these observed changes to the underlying physics of conductivity enhancement and to relevant pathophysiological mechanisms.

This second algorithm was necessary because the occlusion and saline injection were carried out simultaneously; hence, a systematic approach was

required to confirm that the detected effects were indeed due to the injection. This effect is particularly important as it mirrors the anticipated clinical scenario. Both algorithms were validated using numerical simulations.

7.4 Investigating the Pathophysiological Effects of Occlusion and Injection

To better interpret the processed microwave data, pathophysiological aspects of arterial occlusion and saline injection were explored. For short occlusions, the primary cause of asymmetry was presumed to be the difference in blood flow and volume between the two hemispheres of the brain. In contrast, the asymmetry detected during long occlusions was the opposite of that observed during short occlusions, suggesting dynamic fluid redistribution within the brain over time. Among the potential factors responsible for these changes, the early effects of cerebrospinal fluid (CSF) influx were investigated through analysis of CT scans.

7.5 Concluding Remarks and Future Work

This study investigated the microwave-based detection of large vessel occlusion using both short and long arterial occlusions in combination with contralateral saline injections in an animal model. The primary objective was to use the animal model to assess the feasibility of detecting large vessel occlusions in humans preparing for future human clinical trials. A secondary objective involved examining how microwave measurements with contrast enhancement could detect asymmetries in the brain, particularly in the presence of edema formation.

Although the study yielded promising results, it was limited to five animals. Therefore, one must exercise caution in drawing definitive conclusions. Nonetheless, the most significant contribution of this exploratory work is the demonstration that microwave-based detection of large vessel occlusions appears to be feasible and warrants further investigations.

The methods presented here have the potential to improve clinical prehospital diagnostics of large vessel occlusions. It also has the potential to provide insights into the timing and magnitude of pathophysiological developments,

such as edema progression. To confirm the findings of the exploratory work presented in this thesis, future work will involve a study with a fixed protocol, including more animals. If successful, this study could be followed by a clinical human trial.

References

[1] R. Lozano, M. Naghavi, K. Foreman, *et al.*, "Global and regional mortality from 235 causes of death for 20 age groups in 1990 and 2010: A systematic analysis for the global burden of disease study 2010," *The lancet*, vol. 380, no. 9859, pp. 2095–2128, 2012.

[2] C. J. Murray, T. Vos, R. Lozano, *et al.*, "Disability-adjusted life years (dalys) for 291 diseases and injuries in 21 regions, 1990–2010: A systematic analysis for the global burden of disease study 2010," *The lancet*, vol. 380, no. 9859, pp. 2197–2223, 2012.

[3] V. L. Feigin, G. A. Roth, M. Naghavi, *et al.*, "Global burden of stroke and risk factors in 188 countries, during 1990–2013: A systematic analysis for the global burden of disease study 2013," *The Lancet Neurology*, vol. 15, no. 9, pp. 913–924, 2016.

[4] J. Olesen, A. Gustavsson, M. Svensson, *et al.*, "The economic cost of brain disorders in europe," *European journal of neurology*, vol. 19, no. 1, pp. 155–162, 2012.

[5] B. H. Johnson, M. M. Bonafede, and C. Watson, "Short-and longer-term health-care resource utilization and costs associated with acute ischemic stroke," *ClinicoEconomics and outcomes research: CEOR*, vol. 8, p. 53, 2016.

[6] C. Drescher, F. Buchwald, T. Ullberg, M. Pihlsgård, B. Norrving, and J. Petersson, "Epidemiology of first and recurrent ischemic stroke in

sweden 2010–2019: A riksstroke study," *Neuroepidemiology*, vol. 56, no. 6, pp. 433–442, 2023.

[7] Servier Medical Art, https://smart.servier.com/, Accessed: 2025-01-20.

[8] K. N. Sheth, E. E. Smith, M. V. Grau-Sepulveda, D. Kleindorfer, G. C. Fonarow, and L. H. Schwamm, "Drip and ship thrombolytic therapy for acute ischemic stroke: Use, temporal trends, and outcomes," *stroke*, vol. 46, no. 3, pp. 732–739, 2015.

[9] G. Van Belleghem, S. Devos, L. De Wit, *et al.*, "Predicting in-hospital mortality of traffic victims: A comparison between ais-and icd-9-cm-related injury severity scales when only icd-9-cm is reported," *Injury*, vol. 47, no. 1, pp. 141–146, 2016.

[10] N. C. Suwanwela, "Stroke epidemiology in thailand," *Journal of stroke*, vol. 16, no. 1, p. 1, 2014.

[11] R. C. Rennert, A. R. Wali, J. A. Steinberg, *et al.*, "Epidemiology, natural history, and clinical presentation of large vessel ischemic stroke," *Neurosurgery*, vol. 85, no. suppl_1, S4–S8, 2019.

[12] W. G. Kunz, M. G. Hunink, M. A. Almekhlafi, *et al.*, "Public health and cost consequences of time delays to thrombectomy for acute ischemic stroke," *Neurology*, vol. 95, no. 18, e2465–e2475, 2020.

[13] J. M. Wardlaw, V. Murray, E. Berge, and G. J. Del Zoppo, "Thrombolysis for acute ischaemic stroke," *Cochrane database of systematic reviews*, no. 7, 2014.

[14] M. Palaniswami and B. Yan, "Mechanical thrombectomy is now the gold standard for acute ischemic stroke: Implications for routine clinical practice," *Interventional neurology*, vol. 4, no. 1-2, pp. 18–29, 2015.

[15] B. Keselman, A. Berglund, N. Ahmed, *et al.*, "The stockholm stroke triage project: Outcomes of endovascular thrombectomy before and after triage implementation," *Stroke*, vol. 53, no. 2, pp. 473–481, 2022.

[16] J. Thunman, B. Södergård, N. Eckard, C. Nilsson, and S. Hiort, "Hälsoekonomisk utvärdering av trombektomi för behandling av akut svår ischemisk stroke," *Kunskapsunderlag. Stockholm: Tandvårds-och läkemedelsförmånsverket*, 2015.

[17] A. M. Southerland, K. C. Johnston, C. A. Molina, M. H. Selim, N. Kamal, and M. Goyal, "Suspected large vessel occlusion: Should emergency medical services transport to the nearest primary stroke center or bypass to a comprehensive stroke center with endovascular capabilities?" *Stroke*, vol. 47, no. 7, pp. 1965–1967, 2016.

[18] M. Persson, A. Fhager, H. D. Trefná, *et al.*, "Microwave-based stroke diagnosis making global prehospital thrombolytic treatment possible," *IEEE Transactions on Biomedical Engineering*, vol. 61, no. 11, pp. 2806–2817, 2014.

[19] C. Origlia, D. O. Rodriguez-Duarte, J. A. Tobon Vasquez, J.-C. Bolomey, and F. Vipiana, "Review of microwave near-field sensing and imaging devices in medical applications," *Sensors*, vol. 24, no. 14, p. 4515, 2024.

[20] A. Kiourti, A. M. Abbosh, M. Athanasiou, *et al.*, "Next-generation healthcare: Enabling technologies for emerging bioelectromagnetics applications," *IEEE Open Journal of Antennas and Propagation*, vol. 3, pp. 363–390, 2022.

[21] R. Scapaticci, J. Tobon, G. Bellizzi, F. Vipiana, and L. Crocco, "Design and numerical characterization of a low-complexity microwave device for brain stroke monitoring," *IEEE Transactions on Antennas and Propagation*, vol. 66, no. 12, pp. 7328–7338, 2018.

[22] K. B. Walsh, "Non-invasive sensor technology for prehospital stroke diagnosis: Current status and future directions," *International Journal of Stroke*, vol. 14, no. 6, pp. 592–602, 2019.

[23] L. Yang, W. Liu, R. Chen, *et al.*, "In vivo bioimpedance spectroscopy characterization of healthy, hemorrhagic and ischemic rabbit brain within 10 hz–1 mhz," *Sensors*, vol. 17, no. 4, p. 791, 2017.

[24] T. Scheeren, P. Schober, and L. Schwarte, "Monitoring tissue oxygenation by near infrared spectroscopy (nirs): Background and current applications," *Journal of clinical monitoring and computing*, vol. 26, no. 4, pp. 279–287, 2012.

[25] L. di Biase, A. Bonura, M. L. Caminiti, P. M. Pecoraro, and V. Di Lazzaro, "Neurophysiology tools to lower the stroke onset to treatment time during the golden hour: Microwaves, bioelectrical impedance and near infrared spectroscopy," *Annals of Medicine*, vol. 54, no. 1, pp. 2658–2671, 2022.

[26] I. C. Odland, S. Chennareddy, R. Kalagara, *et al.*, "Prehospital stroke detection devices: A bibliometric analysis of current trends," *World Neurosurgery*, vol. 167, e1360–e1375, 2022.

[27] J. C. Maxwell, *A treatise on electricity and magnetism*. Clarendon press, 1873, vol. 1.

[28] A. Vander Vorst, A. Rosen, and Y. Kotsuka, *RF/microwave interaction with biological tissues*. John Wiley & Sons, 2006.

[29] D. M. Pozar, *Microwave engineering*. John wiley & sons, 2011.

[30] M. Guardiola, S. Capdevila, J. Romeu, and L. Jofre, "3-d microwave magnitude combined tomography for breast cancer detection using realistic breast models," *IEEE antennas and wireless propagation letters*, vol. 11, pp. 1622–1625, 2012.

[31] S. Hosseinzadegan, A. Fhager, M. Persson, S. D. Geimer, and P. M. Meaney, "Discrete dipole approximation-based microwave tomography for fast breast cancer imaging," *IEEE Transactions on Microwave Theory and Techniques*, vol. 69, no. 5, pp. 2741–2752, 2021.

[32] K. Smith, J. Bourqui, Z. Wang, *et al.*, "Microwave imaging for monitoring breast cancer treatment: A pilot study," *Medical physics*, vol. 50, no. 11, pp. 7118–7129, 2023.

[33] V. Mattsson, L. L. Ackermans, B. Mandal, *et al.*, "Mas: Standalone microwave resonator to assess muscle quality," *Sensors*, vol. 21, no. 16, p. 5485, 2021.

[34] A. Garrido-Atienza, M. Guardiola, L. M. Neira, J. Romeu, and A. Fhager, "Movement tracking and false positive reduction method for microwave colonoscopy systems," *IEEE Journal of Electromagnetics, RF and Microwaves in Medicine and Biology*, 2024.

[35] D. Ireland and M. Bialkowski, "Microwave head imaging for stroke detection," *Progress In Electromagnetics Research M*, vol. 21, pp. 163–175, 2011.

[36] A. Fhager, S. Candefjord, M. Elam, and M. Persson, "Microwave diagnostics ahead: Saving time and the lives of trauma and stroke patients," *IEEE Microwave Magazine*, vol. 19, no. 3, pp. 78–90, 2018.

[37] A. Fhager, S. Candefjord, M. Elam, and M. Persson, "3d simulations of intracerebral hemorrhage detection using broadband microwave technology," *Sensors*, vol. 19, no. 16, p. 3482, 2019.

[38] R. Hood, M. Persson, A. Fhager, *et al.*, "Evaluating the sensitivity and specificity of a microwave based tool to support and enhance stroke triage," in *INTERNATIONAL JOURNAL OF STROKE*, SAGE PUBLICATIONS LTD 1 OLIVERS YARD, 55 CITY ROAD, LONDON EC1Y 1SP, ENGLAND, vol. 17, 2022, pp. 64–65.

[39] M. Hopfer, R. Planas, A. Hamidipour, T. Henriksson, and S. Semenov, "Electromagnetic tomography for detection, differentiation, and monitoring of brain stroke: A virtual data and human head phantom study.," *IEEE Antennas and Propagation Magazine*, vol. 59, no. 5, pp. 86–97, 2017.

[40] J. A. Tobon Vasquez, R. Scapaticci, G. Turvani, *et al.*, "A prototype microwave system for 3d brain stroke imaging," *Sensors*, vol. 20, no. 9, p. 2607, 2020.

[41] A. Brankovic, A. Zamani, A. Trakic, *et al.*, "Unsupervised algorithm for brain anomalies localization in electromagnetic imaging," *IEEE Transactions on Computational Imaging*, vol. 6, pp. 1595–1606, 2020.

[42] U. Anwar, S. Khan, T. Arslan, T. C. Russ, and P. Lomax, "Radio frequency-enabled cerebral blood flow monitoring and classification using data augmentation and machine learning techniques," *IEEE Sensors Journal*, 2024.

[43] *Medfield diagnostics ab*, `https://www.medfielddiagnostics.com/`.

[44] S. Semenov, T. Huynh, T. Williams, B. Nicholson, and A. Vasilenko, "Dielectric properties of brain tissue at 1 ghz in acute ischemic stroke: Experimental study on swine.," *Bioelectromagnetics*, vol. 38, no. 2, pp. 158–163, 2016.

[45] R. Scapaticci, O. Bucci, I. Catapano, and L. Crocco, "Differential microwave imaging for brain stroke followup," *International Journal of Antennas and Propagation*, vol. 2014, 2014.

[46] D. O. Rodriguez-Duarte, J. A. T. Vasquez, R. Scapaticci, L. Crocco, and F. Vipiana, "Assessing a microwave imaging system for brain stroke monitoring via high fidelity numerical modelling," *IEEE Journal of Electromagnetics, RF and Microwaves in Medicine and Biology*, vol. 5, no. 3, pp. 238–245, 2021.

[47] O. Karadima, P. Lu, I. Sotiriou, and P. Kosmas, "Experimental validation of the dbim-twist algorithm for brain stroke detection and differentiation using a multi-layered anatomically complex head phantom," *IEEE Open Journal of Antennas and Propagation*, vol. 3, pp. 274–286, 2022.

[48] D. Carr, J. Brown, G. Bydder, *et al.*, "Gadolinium-dtpa as a contrast agent in mri: Initial clinical experience in 20 patients," *American Journal of Roentgenology*, vol. 143, no. 2, pp. 215–224, 1984.

[49] J. S. Hudson, T. K. Chung, B. S. Prout, Y. Nagahama, M. L. Raghavan, and D. M. Hasan, "Iron nanoparticle contrast enhanced microwave imaging for emergent stroke: A pilot study," *Journal of Clinical Neuroscience*, vol. 59, pp. 284–290, 2019.

[50] R. Lahri, M. Rahman, M. Wright, P. Kosmas, and M. Thanou, "Zinc oxide nanoparticles as contrast-enhancing agents for microwave imaging," *Medical physics*, vol. 45, no. 8, pp. 3820–3830, 2018.

[51] S. Coşğun, E. Bilgin, and M. Çayören, "Microwave imaging of breast cancer with factorization method: Spions as contrast agent," *Medical Physics*, vol. 47, no. 7, pp. 3113–3122, 2020.

[52] A. Madannejad, J. EbrahimiZadeh, F. Ravanbakhsh, M. D. Perez, and R. Augustine, "Reflectometry enhancement by saline injection in microwave-based skin burn injury diagnosis," in *2020 14th European Conference on Antennas and Propagation (EuCAP)*, IEEE, 2020, pp. 1–4.

[53] S. M. Pishnamaz, "Towards microwave detection of thromboses," Licentiate Thesis, Chalmers University of Technology, 2022.

[54] G. Van Rhoon, P. Rietveld, and J. Van der Zee, "A 433 mhz lucite cone waveguide applicator for superficial hyperthermia," *International journal of hyperthermia*, vol. 14, no. 1, pp. 13–27, 1998.

[55] P. Togni, Z. Rijnen, W. Numan, *et al.*, "Electromagnetic redesign of the hypercollar applicator: Toward improved deep local head-and-neck hyperthermia," *Physics in Medicine & Biology*, vol. 58, no. 17, p. 5997, 2013.

[56] P. Takook, M. Persson, J. Gellermann, and H. D. Trefná, "Compact self-grounded bow-tie antenna design for an uwb phased-array hyperthermia applicator," *International Journal of Hyperthermia*, vol. 33, no. 4, pp. 387–400, 2017.

[57] M. Ghaderi Aram, H. Aliakbarian, and H. Dobšíček Trefná, "An ultra-wideband compact design for hyperthermia: Open ridged-waveguide antenna," *IET Microwaves, Antennas & Propagation*, vol. 16, no. 2-3, pp. 137–152, 2022.

[58] X. Li, *Body matched antennas for microwave medical applications*. KIT Scientific Publishing, 2014, vol. 72.

[59] M. L. Scarpello, D. Kurup, H. Rogier, *et al.*, "Design of an implantable slot dipole conformal flexible antenna for biomedical applications," *IEEE transactions on antennas and propagation*, vol. 59, no. 10, pp. 3556–3564, 2011.

[60] S. M. Aguilar, M. A. Al-Joumayly, M. J. Burfeindt, N. Behdad, and S. C. Hagness, "Multiband miniaturized patch antennas for a compact, shielded microwave breast imaging array," *IEEE transactions on antennas and propagation*, vol. 62, no. 3, pp. 1221–1231, 2013.

[61] X. Li, M. Jalilvand, Y. L. Sit, and T. Zwick, "A compact double-layer on-body matched bowtie antenna for medical diagnosis," *IEEE transactions on antennas and propagation*, vol. 62, no. 4, pp. 1808–1816, 2014.

[62] J. M. Felício, J. M. Bioucas-Dias, J. R. Costa, and C. A. Fernandes, "Antenna design and near-field characterization for medical microwave imaging applications," *IEEE Transactions on Antennas and Propagation*, vol. 67, no. 7, pp. 4811–4824, 2019.

[63] M. Rokunuzzaman, A. Ahmed, T. C. Baum, and W. S. Rowe, "Compact 3-d antenna for medical diagnosis of the human head," *IEEE Transactions on Antennas and Propagation*, vol. 67, no. 8, pp. 5093–5103, 2019.

[64] D. O. Rodriguez-Duarte, J. A. T. Vasquez, R. Scapaticci, L. Crocco, and F. Vipiana, "Brick-shaped antenna module for microwave brain imaging systems," *IEEE Antennas and Wireless Propagation Letters*, vol. 19, no. 12, pp. 2057–2061, 2020.

[65] O. Fiser, V. Hruby, J. Vrba, *et al.*, "Uwb bowtie antenna for medical microwave imaging applications," *IEEE Transactions on Antennas and Propagation*, 2022.

[66] U. Rafique, S. Pisa, R. Cicchetti, O. Testa, and M. Cavagnaro, "Ultra-wideband antennas for biomedical imaging applications: A survey," *Sensors*, vol. 22, no. 9, p. 3230, 2022.

[67] H. Chen and K.-M. Luk, "An on-body matched differentially fed magnetoelectric dipole antenna for head imaging systems," *IEEE Transactions on Antennas and Propagation*, vol. 70, no. 11, pp. 10 032–10 046, 2022.

[68] S. M. H. Mousavi, K. Sultan, L. Guo, A. S. Janani, K. Bialkowski, and A. M. Abbosh, "Dual-sense circularly polarized substrate integrated waveguide antenna for deep torso imaging," *IEEE Transactions on Antennas and Propagation*, 2024.

[69] T. Alves, B. Poussot, and J.-M. Laheurte, "Analytical propagation modeling of ban channels based on the creeping-wave theory," *IEEE Transactions on Antennas and Propagation*, vol. 59, no. 4, pp. 1269–1274, 2010.

[70] P. M. Meaney, F. Shubitidze, M. W. Fanning, M. Kmiec, N. R. Epstein, and K. D. Paulsen, "Surface wave multipath signals in near-field microwave imaging," *International journal of biomedical imaging*, vol. 2012, 2012.

[71] H. Dobšíček Trefná, J. Vrba, and M. Persson, "Evaluation of a patch antenna applicator for time reversal hyperthemia," *International Journal of Hyperthermia*, vol. 26, no. 2, pp. 185–197, 2010.

[72] J. Yang and A. Kishk, "A novel low-profile compact directional ultra-wideband antenna: The self-grounded bow-tie antenna," *IEEE Transactions on Antennas and Propagation*, vol. 60, no. 3, pp. 1214–1220, 2011.

[73] T. W. Eigentler, L. Winter, H. Han, *et al.*, "Wideband self-grounded bow-tie antenna for thermal mr," *NMR in Biomedicine*, vol. 33, no. 5, e4274, 2020.

[74] S. M. Pishnamaz, X. Zeng, H. D. Trefná, M. Persson, and A. Fhager, "Reducing waves on the body surface in near-field medical diagnostics by a dielectric rod antenna," *IEEE Transactions on Antennas and Propagation*, vol. 71, no. 10, pp. 7958–7969, 2023.

[75] R. Kazemi, A. E. Fathy, and R. A. Sadeghzadeh, "Dielectric rod antenna array with substrate integrated waveguide planar feed network for wideband applications," *IEEE Transactions on Antennas and Propagation*, vol. 60, no. 3, pp. 1312–1319, 2012.

[76] A. Safaai-Jazi and G. Yip, "Classification of hybrid modes in cylindrical dielectric optical waveguides," *Radio Science*, vol. 12, no. 4, pp. 603–609, 1977.

[77] C. A. Balanis, *Advanced engineering electromagnetics*. John Wiley & Sons, 2012.

[78] G. Strang, G. Strang, G. Strang, and G. Strang, *Introduction to linear algebra*. Wellesley-Cambridge Press Wellesley, MA, 1993, vol. 3.

[79] K. Y. Kim, H.-S. Tae, J.-H. Lee, and H.-S. Kim, "Analysis of dielectric loss in three-region all dielectric circular waveguides," *KIEE International Transactions on Electrophysics and Applications*, vol. 12, no. 3, pp. 181–185, 2002.

[80] Mathworks, *Mldivide*, `https://se.mathworks.com/help/matlab/ref/mldivide.html`, Accessed: 2022-12-09.

[81] A. Snyder, "Surface waveguide modes along a semi-infinite dielectric fiber excited by a plane wave," *JOSA*, vol. 56, no. 5, pp. 601–606, 1966.

[82] G. L. Yip, "Launching efficiency of the he/sub 11/surface wave mode on a dielectric rod," *IEEE Transactions on Microwave Theory and Techniques*, vol. 18, no. 12, pp. 1033–1041, 1970.

[83] F. Wang, H. Zhang, J. Bao, *et al.*, "Experimental study on differential diagnosis of cerebral hemorrhagic and ischemic stroke based on microwave measurement," *Technology and Health Care*, vol. 28, no. S1, pp. 289–301, 2020.

[84] Z. Lv, L. Zeng, Z. Wang, *et al.*, "A symmetrical independent antenna pair sensor for dynamic monitoring of ischemia stroke," *Measurement*, vol. 239, p. 115 431, 2025.

[85] A. Banstola and J. N. Reynolds, "Mapping sheep to human brain: The need for a sheep brain atlas," *Frontiers in Veterinary Science*, vol. 9, p. 961 413, 2022.

[86] J. Boltze, A. Förschler, B. Nitzsche, *et al.*, "Permanent middle cerebral artery occlusion in sheep: A novel large animal model of focal cerebral ischemia," *Journal of Cerebral Blood Flow & Metabolism*, vol. 28, no. 12, pp. 1951–1964, 2008.

[87] A. Taha, J. Bobi, R. Dammers, *et al.*, "Comparison of large animal models for acute ischemic stroke: Which model to use?" *Stroke*, vol. 53, no. 4, pp. 1411–1422, 2022.

[88] The Royal Norwegian Ministry of Agriculture and Food, *Regulations on the use of animals in experiments*, `https://lovdata.no/dokument/SF/forskrift/2015-06-18-761`, 2015.

[89] The Royal Norwegian Ministry of Agriculture and Food, *Amendment of the regulations on the use of animals in experiments*, `https://lovdata.no/static/lovtidend/ltavd1/2017/sf-20170405-0451.pdf`, 2017.

[90] Norwegian National Committee for Research Ethics in Science and Technology, *Ethical guidelines for the use of animals in research*, `https://www.forskningsetikk.no/en/guidelines/science-and-technology/ethical-guidelines-for-the-use-of-animals-in-research/`.

[91] Norwegian Food Safety Authority (Mattilsynet), *Testing of a "strokefinder" on sheep- a pilot trial*, `https://www.mattilsynet.no/dyr/forsoksdyr/soknader?bId=19742`, Reference Number: [19742], 2019.

[92] Norwegian Food Safety Authority (Mattilsynet), *Testing of a "strokefinder" on sheep*, `https://www.mattilsynet.no/dyr/forsoksdyr/soknader?bId=28659`, Reference Number: [28659], 2022.

[93] S. Ghosal and K. N. Sheth, *Cerebral Edema and Intracranial Pressure in the Neurocritical Care Unit*. Cambridge University Press, 2019.

[94] A. J. Wells, R. Vink, P. C. Blumbergs, *et al.*, "A surgical model of permanent and transient middle cerebral artery stroke in the sheep," *PLOS ONE*, 2012.

[95] B. Baldwin and F. Bell, "The effect of temporary reduction in cephalic blood flow on the eeg of sheep and calf," *Electroencephalography and clinical Neurophysiology*, vol. 15, no. 3, pp. 465–473, 1963.

[96] N. May, "Experimental studies of the collateral circulation in the head and neck of sheep (ovis aries).," *Journal of Anatomy*, vol. 103, no. Pt 1, p. 171, 1968.

[97] Z. Qian, S. Climent, M. Maynar, *et al.*, "A simplified arteriovenous malformation model in sheep: Feasibility study," *American journal of neuroradiology*, vol. 20, no. 5, pp. 765–770, 1999.

[98] S. Terlecki, B. Baldwin, and F. Bell, "Experimental cerebral ischaemia in sheep: Neuropathology and clinical effects," *Acta neuropathologica*, vol. 7, pp. 185–200, 1967.

[99] J. Bardutzky and S. Schwab, "Antiedema therapy in ischemic stroke," *Stroke*, vol. 38, no. 11, pp. 3084–3094, 2007.

[100] Keysight, *N7081a microwave transceiver*, `https://www.keysight.com/se/en/assets/9018-04678/technical-specifications/9018-04678.pdf`.

[101] S. M. Pishnamaz, X. Zeng, H. D. Trefná, M. Persson, and A. Fhager, "Asymmetry detection in a noisy microwave-based biomedical diagnosis," in *2024 IEEE MTT-S International Microwave Biomedical Conference (IMBioC)*, IEEE, 2024, pp. 12–14.

[102] S. M. Kay, *Fundamentals of Statistical Signal Processing: Estimation Theory*. Prentice Hall, 1993.

[103] J. M. Donadille and O. Faivre, "Water complex permittivity model for dielectric logging," in *SPE Middle East Oil and Gas Show and Conference*, SPE, 2015, SPE–172 566.

[104] A. Peyman, C. Gabriel, and E. Grant, "Complex permittivity of sodium chloride solutions at microwave frequencies," *Bioelectromagnetics: Journal of the Bioelectromagnetics Society, The Society for Physical Regulation in Biology and Medicine, The European Bioelectromagnetics Association*, vol. 28, no. 4, pp. 264–274, 2007.

[105] S. M. Pishnamaz, X. Zeng, H. D. Trefná, M. Persson, and A. Fhager, "Microwave-based detection of ischemic stroke using contrast enhancement," *To be Submitted to IEEE Transactions on Biomedical Engineering*, 2025.

[106] R. J. Hodrick and E. C. Prescott, "Postwar us business cycles: An empirical investigation," *Journal of Money, credit, and Banking*, pp. 1–16, 1997.

[107] B. Baldwin and F. Bell, "Blood flow in the carotid and vertebral arteries of the sheep and calf," *The Journal of Physiology*, vol. 167, no. 3, p. 448, 1963.

[108] H. Mestre, T. Du, A. M. Sweeney, *et al.*, "Cerebrospinal fluid influx drives acute ischemic tissue swelling," *Science*, vol. 367, no. 6483, eaax7171, 2020.

[109] T. Du, H. Mestre, B. T. Kress, *et al.*, "Cerebrospinal fluid is a significant fluid source for anoxic cerebral oedema," *Brain*, vol. 145, no. 2, pp. 787–797, 2022.

[110] B. A. Plog, H. Mestre, G. E. Olveda, *et al.*, "Transcranial optical imaging reveals a pathway for optimizing the delivery of immunotherapeutics to the brain," *JCI insight*, vol. 3, no. 20, 2018.

[111] T. O. Lilius, M. Rosenholm, L. Klinger, *et al.*, "Spect/ct imaging reveals cns-wide modulation of glymphatic cerebrospinal fluid flow by systemic hypertonic saline," *Iscience*, vol. 25, no. 10, 2022.

[112] P. A. Bork, M. Gianetto, E. Newbold, L. Hablitz, T. Bohr, and M. Nedergaard, "Blood osmolytes such as sugar can drive brain fluid flows in a poroelastic model," *Scientific Reports*, vol. 14, no. 1, p. 29 017, 2024.

[113] N. J. Abbott, A. A. Patabendige, D. E. Dolman, S. R. Yusof, and D. J. Begley, "Structure and function of the blood–brain barrier," *Neurobiology of disease*, vol. 37, no. 1, pp. 13–25, 2010.

[114] A. Monro, *Observations on the structure and functions of the nervous system*. Classics of Neurology & Neurosurgery Library Division of Gryphon Editions, 1994.

[115] G. Kellie, "An account of the appearances observed in the dissection of two of three individuals presumed to have perished in the storm of the 3d, and whose bodies were discovered in the vicinity of leith on the morning of the 4th, november 1821; with some reflections on the pathology of the brain: Part i," *Transactions. Medico-Chirurgical Society of Edinburgh*, vol. 1, p. 84, 1824.

[116] J. Badaut and N. Plesnila, *Brain Edema: From Molecular Mechanisms to Clinical Practice*. Academic Press, 2017, ch. 12.

[117] B. Baldwin and F. Bell, "The anatomy of the cerebral circulation of the sheep and ox. the dynamic distribution of the blood supplied by the carotid and vertebral arteries to cranial regions," *Journal of anatomy*, vol. 97, no. Pt 2, p. 203, 1963.

[118] Y.-Y. Lee, I. Choi, S.-J. Lee, *et al.*, "Clinical significance of gray to white matter ratio after cardiopulmonary resuscitation in children," *Children*, vol. 9, no. 1, p. 36, 2022.

[119] B. Nitzsche, S. Frey, L. D. Collins, *et al.*, "A stereotaxic, population-averaged t1w ovine brain atlas including cerebral morphology and tissue volumes," *Frontiers in neuroanatomy*, vol. 9, p. 69, 2015.

[120] Q. Han, J. Yang, X. Gao, *et al.*, "Early edema within the ischemic core is time-dependent and associated with functional outcomes of acute ischemic stroke patients," *Frontiers in Neurology*, vol. 13, p. 861 289, 2022.